# Capabilities of a multi-pinhole SPECT system with two stationary detectors for in vivo imaging in rodents

-

# Leistungsfähigkeit eines Multi-Pinhole SPECT-Systems mit zwei stationären Detektoren zur In-vivo-Bildgebung in Nagetiermodellen

Doctoral thesis for a medical doctoral degree
at the Graduate School of Life Sciences,
Julius-Maximilians-Universität Würzburg,
Section Clinical Sciences

submitted by

**Jan Paul Janßen**

from

**Erlangen**

**Würzburg 2023**

**Submitted on: ……..…….**

Office stamp

## Members of the Thesis Committee:

**Chairperson:** **Prof. Dr. rer. nat. Klaus Brehm**

**Primary Supervisor:** **Prof. Dr. med. Andreas Buck**

**Supervisor (Second):** **Prof. Takahiro Higuchi, MD, PhD**

**Supervisor (Third):** **Prof. Dr. rer. nat. Herbert Köstler**

Date of Public Defence: ……..……

Date of Receipt of Certificates: …….

# Table of contents

# 1 Introduction

Molecular imaging of small animals is essential in preclinical research [1-3]. Radionuclide imaging that includes single-photon emission computed tomography (SPECT) and positron emission tomography (PET) plays a vital role [4, 5]. Especially in combination with other modalities, such as computed tomography (CT) or magnetic resonance imaging (MRI), these techniques provide valuable information about health status [6-8]. In the field of SPECT, there have been major innovations in recent years so that image quality and diagnostic accuracy has been improved significantly [9-11]. Using gamma cameras with adequate collimators, even tiny amounts of radioactive substances can be detected with good spatial resolution. Particularly for small target volumes such as rodents, the introduction of single-pinhole and, further, multi-pinhole collimators has led to resolutions of less than one millimeter with acceptable sensitivity [12, 13]. Further advantages, such as the wide availability of suitable radioisotopes and the ability to image multiple radioisotopes simultaneously, are unique features of SPECT compared to PET [4].

In this thesis, a dedicated small animal SPECT system with stationary detectors and multi-pinhole collimation providing a fixed field of view (FOV) through which the target volume is moved stepwise is investigated. This technology allows dynamic examinations with high accuracy and reduces mechanical problems that can occur in conventional systems with moving detectors [14, 15]. Previous generations typically had three detectors arranged triangularly around the central collimator [11, 16]. The system under study was designed to be more cost-efficient by omitting the lower detector. High resolution with good image quality is required for scans to provide high diagnostic value. In addition to the detectors and the collimators used [17], the reconstruction algorithm [18, 19], the post-filter [18], and the injection dose or scan time [20] also impact the results. Therefore, a wide range of activity concentrations with different post-filters was analyzed using the new iterative reconstruction algorithm similarity-regulated ordered-subsets expectation maximization (SROSEM) [21]. This algorithm allows for accelerated reconstruction at constant reconstruction parameters without significantly compromising image quality.

Rats and mice are the most popular animal models in basic and translational research to study pathophysiology and develop new drugs [2]. Rats have certain advantages over mice [22, 23]. Many studies on the performance and image quality of comparable SPECT

systems are performed only in mice [10, 11], which does not do justice to the enormously important role of rats in preclinical research. Therefore, it was focused on imaging in rats.

This thesis aims to investigate the performance of the new micro-SPECT system with two stationary detectors and a preset SROSEM reconstruction algorithm in combination with Gaussian post-filtering in rats. For this purpose, clinically relevant myocardial perfusion and bone SPECT studies were carried out with $^{99m}$Tc sesta-methoxyisobutylisonitrile ($^{99m}$Tc-MIBI) [24] and $^{99m}$Tc hydroxymethylene diphosphonate ($^{99m}$Tc-HMDP) [25, 26], respectively.

## Remark

The methods and results of this dissertation have already been published in *Scientific Reports* (2020) [27]. Since this publication follows the Creative Commons Attribution 4.0 International License (https://creativecommons.org/licenses/by/4.0/), redistribution and adaptation are permitted as long as the source is appropriately cited. Copyright belongs to the authors (Janssen JP et al.).

## 1.1 Molecular imaging

"Molecular imaging is the visualization, characterization, and measurement of biological processes at the molecular and cellular levels in humans and other living systems. To elaborate: Molecular imaging typically includes 2- or 3-dimensional imaging as well as quantification over time. The techniques used include radiotracer imaging/nuclear medicine, MR imaging, MR spectroscopy, optical imaging, ultrasound, and others." as defined by Mankoff et al. [28].

Nuclear medicine examinations such as PET and SPECT are crucial due to their wide range of applications using radiotracers. The application areas can be diverse, from oncological, cardiological, and neurological to orthopedic issues and many more [29]. Most conventional X-ray, ultrasound, or magnetic resonance-based techniques provide morphological information with high spatial resolution, but no functional insights are registered (e.g. metabolic processes, surface antigens, other genetic transcripts, or protein-protein interactions) [30]. Thus, conventional and molecular imaging can be complementary in many applications, as reflected in the success of hybrid imaging [7, 8, 31, 32].

The relevance of molecular imaging arises from the ability to detect diseases at early stages, assess the extent of diseases, avoid or replace invasive diagnostics, and even help select a specific therapy (keyword: personalized medicine) [30]. In addition, standardized methods also allow noninvasive therapy monitoring, measuring the response to a particular treatment long before the tumor shrinks morphologically, for example [33].

## 1.2 Molecular imaging of small animals

While SPECT was initially developed for human applications, the technology has been adapted for small-animal applications in recent decades [3]. Small-animal molecular imaging for basic and translational research has grown tremendously. The steady increase of animal models such as transgenic mouse and rat models has made emission imaging an indispensable part of preclinical research [5, 34, 35].

Following the publication of Massoud and Gambhir [1], the areas of application in biomedical research include the development of new noninvasive imaging techniques to visualize specific cellular and molecular processes (e.g., tracer development, in vivo tracking of cell migration and interaction, improvement of drug and gene therapy, imaging of drug effects at the molecular and cellular level, monitoring of disease progression and

impact of treatments in vivo, visualization of multiple molecular events simultaneously and more).

Studying the living subject allows the full complexity of its biology to be considered and observed over time [1]. Before molecular imaging was established in preclinical research, more experimental animals had to be killed at different times during a study to obtain longitudinal information. Moreover, there was no possibility to compare the same animal to itself. Thus, imaging helps to reduce the use of laboratory animals and to improve the comparability and validity of information in longitudinal studies [4]. To exploit these potentials, it is crucial that the underlying technology is easy to operate, quantifiable, and provides reproducible results [1]. Molecular imaging is highly translational and represents an important interface for the transfer of preclinical to clinical research and, ultimately, for improving healthcare [4, 6]. For example, oncology imaging as well as respective treatment could be decisively improved [34, 36].

Another important point is that technical development uses preclinical imaging as a testing ground for innovations. Rather than adapting technologies from the clinic to small animals, innovations can be tested in small animals, improving biomedical research and, in the long run, human imaging in clinical practice [37].

In summary, molecular and multimodality imaging has become indispensable in preclinical research. The physical principles behind each modality are essential for proper use. To allow comparability of studies, further development of imaging technology and standardization of imaging protocols are imperative scientific goals [6].

## 1.3 Rodent models

Rodents have always been prevalent animal models in biomedical research. In recent years the focus has increasingly shifted to the mouse, as it was possible to introduce a transgenic model and the first knockout animal much earlier than in the rat [23]. However, due to advances in genetic technology, this lead is fading with the introduction of more and more new rat models [38].

Rats have several advantages over mice [23]. On the one hand, their size makes it easier to perform invasive procedures such as surgery or hemodynamic measurements. On the other hand, they also provide more tissue for histological and biological analyses [22]. They have brains four times larger than mice, a much bigger frontal cord [39] and some physiological processes and behaviors can so far only be established in the rat model [23]. For example, the respective rat model has proven its superiority in addiction

research [40]. Looking at research in pharmacology and toxicology rat models are also considered the gold standard [38].

For molecular imaging, the size of the rats is advantageous, as a lower resolution is required to image the same structures as in mice. At the same time, the larger bodies also lead to increased soft tissue attenuation and scattering [41]. In addition, the investigated SPECT system requires a larger transaxial diameter of the collimator. Thus, the magnification ratio between the scanned animal and the detector projection becomes lower.

The numerous advantages of the rat over the mice model and particularly the fact that many performance evaluations have been conducted only in dedicated mouse configurations prompted us to investigate the imaging capabilities for rats [10, 11, 18, 42].

## 1.4 The tracer principle

“The tracer principle is the study of the fate of compounds in vivo using minute amounts of radioactive tracers which do not elicit any pharmacological response by the body to the tracer.” as defined in “Nuclear Medicine Physics: A Handbook for Teachers and Students” by Bailey et al. [43].

Tracers are usually composed of two parts: a pharmacophore and a chelating group for the radiometal [44]. A chemical linker connects these two parts to form a radioactive conjugated complex. To image the tracers, the gamma radiation generated by them is necessary. In this context, gamma radiation from excited atomic nuclei must be differentiated from gamma radiation due to annihilation [43]. The gamma photons of an excited atomic nucleus are produced when the atomic nucleus emits excess energy to change to a more energetically favorable state. This can occur, for example, after a radioactive decay. These gamma photons have a characteristic energy spectrum depending on the origin of excitation of the nucleus and which element it is. Detection of these photons is the fundamental of scintigraphy and SPECT. In contrast, PET relies on gamma photons deriving from an annihilation event of two particles (usually electron and positron). This is done using radioisotopes that follow the $\beta^+$ decay and emit positrons that collide with electrons in the environment and annihilate, emitting two gamma photons at 511 keV in opposite directions.

The most common radioisotope is $^{99m}$Tc [43]. It is one of those used for scintigraphic imaging, which emits gamma photons by changing the state of the excited nucleus. The

peculiarity of $^{99m}$Tc is that it is a metastable isotope that remains for a relatively long period of time excited, so the emission of gamma rays occurs later after the underlying $\beta^-$ decay. It is very well studied and is available as a component of many tracers. Potential applications include imaging of the thyroid, bones, lungs, heart, brain, kidneys and many more [45].

$^{99m}$Tc is produced commercially using nuclear reactors to create $^{99}$Mo from $^{235}$U, with a half-life of about 66h [46]. This is distributed in the form of $^{99m}$Tc generators. These were developed at Brookhaven National Laboratory in the 1950s and were first suggested as a medical tracer in 1960 [47, 48]. Within these generators, the decay of $^{99}$Mo via $^{99m}$Tc to $^{99}$Tc takes place. By column chromatography, the $^{99m}$Tc can be isolated and extracted as pertechnetate. Subsequently, the obtained $^{99m}$Tc-pertechnetate can be used for imaging or bound to another molecule using a tracer kit. The obtained $^{99m}$Tc has a half-life of about 6 h until it decays to $^{99}$Tc by emitting gamma rays with an energy of 140.5 keV [46]. $^{99}$Tc has a long half-life of 211,000 a until it decays to the stable $^{99}$Ru. The entire decay process is shown in ***Figure 1***.

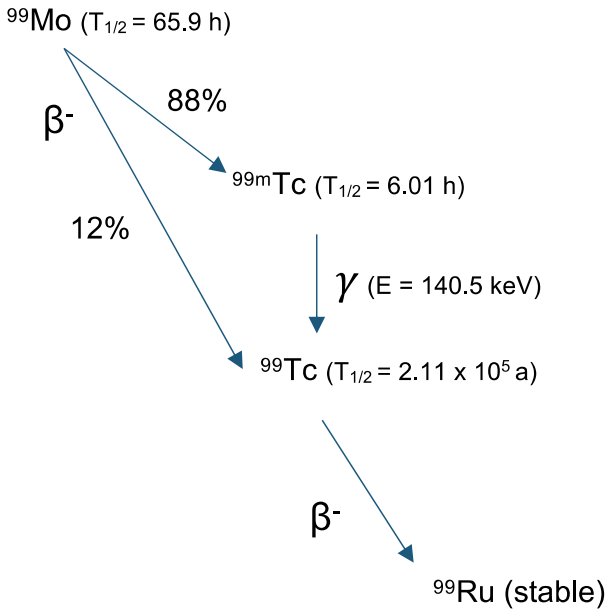


***Figure 1*** *Decay of molybdenum-99*

*$^{99}$Mo decays with a half-life of 65.9 h to 88% to $^{99m}$Tc and 12% to $^{99}$Tc [46]. The metastable technetium releases its excess energy with a half-life of 6.01h in the form of gamma rays and thus also becomes $^{99}$Tc. These gamma rays with an energy of 140.5 keV are used for imaging. The $^{99}$Tc decays with a half-life of 2.11 x $10^5$ a to the stable $^{99}$Ru. Own illustration.*

These properties make it a well-suited isotope for living organisms since it gets by with moderate radiation exposure and does not pose a severe environmental threat. In addition, it can be made widely available through generators containing a precursor and not rely on on-site production, unlike most PET tracers that require a cyclotron. Because $^{99m}$Tc has been known for decades, there is an extensive range of tracers, and the research in development of new technetium-based tracers is well established [49].
$^{99m}$Tc remains the most commonly employed radiotracer, and the number of examinations by far exceeds the number of those performed with PET tracers. $^{99m}$Tc is a radioisotope that has contributed most to the worldwide spread of nuclear medicine and is used in about 85% of all nuclear medicine examinations [50-53].
Altogether, this demonstrates the relevance of $^{99m}$Tc and is also the reason why the following work is based on measurements with $^{99m}$Tc-based tracers.

### 1.4.1 Applied tracers

In the following, the tracers used in this work are briefly presented: $^{99m}$Tc-pertechnetate, -HMDP, and -MIBI. $^{99m}$Tc-pertechnetate is mainly used for thyroid imaging, $^{99m}$Tc-HMDP for skeletal imaging, and $^{99m}$Tc-MIBI for cardiac imaging [45]. These tracers are among the most widely used for SPECT imaging and together cover a large fraction of the nuclear medicine examinations performed in Germany and worldwide (***Figure 2***) [54]. The figure also highlights the current importance of SPECT over PET, even though the number of PET examinations has increased significantly since data collection and continues to do so.

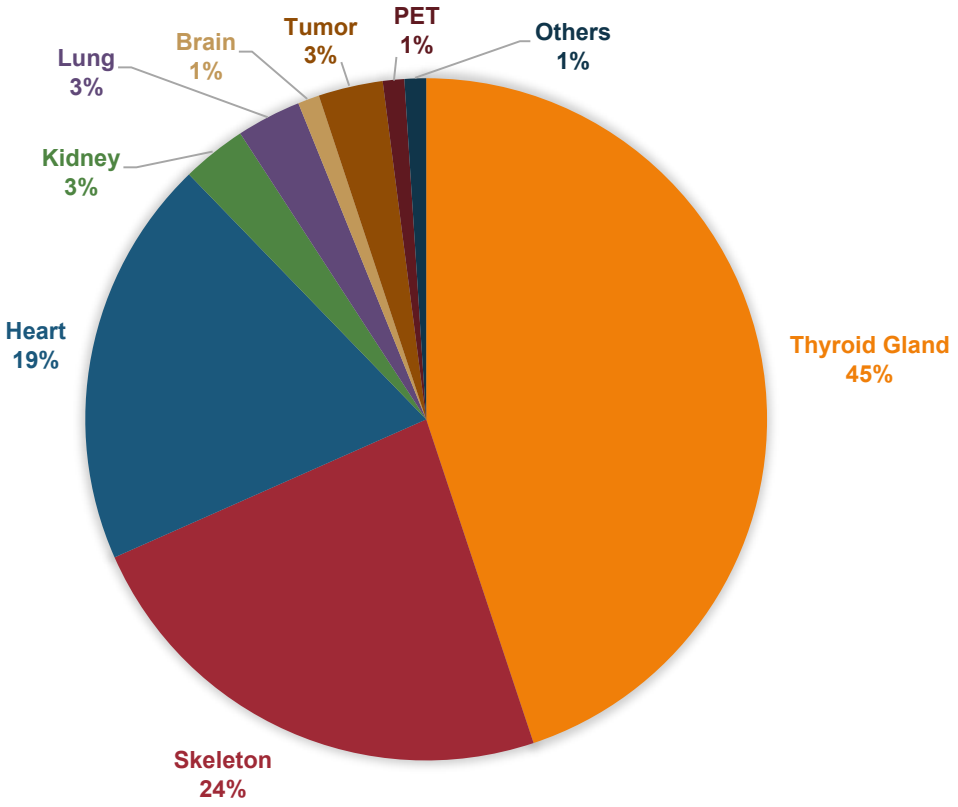


***Figure 2*** *Shares of nuclear medicine examinations in Germany 2016*

*Three examinations are predominating: thyroid scintigraphy, bone scintigraphy, and cardiac scintigraphy. It should be noted that rest and stress myocardial scintigraphy are separately counted in the statistics. Own illustration based on the website of the "Bundesamt für Strahlenschutz" (Federal Office for Radiation Protection) [54].*

### 1.4.2 $^{99m}$Tc-pertechnetate

$^{99m}$Tc-pertechnetate is a tracer consisting of an oxyanion with the formula $TcO_4^-$ [55]. The structural formula is shown in ***Figure 3A***. It is straightforward to obtain, as it can be received in its form from the technetium generator and does not require any specific preparation using a dedicated kit. In nuclear medicine, $^{99m}$Tc-pertechnetate is extremely versatile as it is distributed in the body to a similar extent as iodine. It is the most employed radiopharmaceutical for thyroid scintigraphy and has several advantages over iodine-based tracers. Besides the thyroid gland, it also accumulates in the salivary glands, gastric mucosa, and choroid plexus.

For performance measurements, $^{99m}$Tc-pertechnetate is standard [42, 56], which is why it was used for all phantom scans in this thesis.

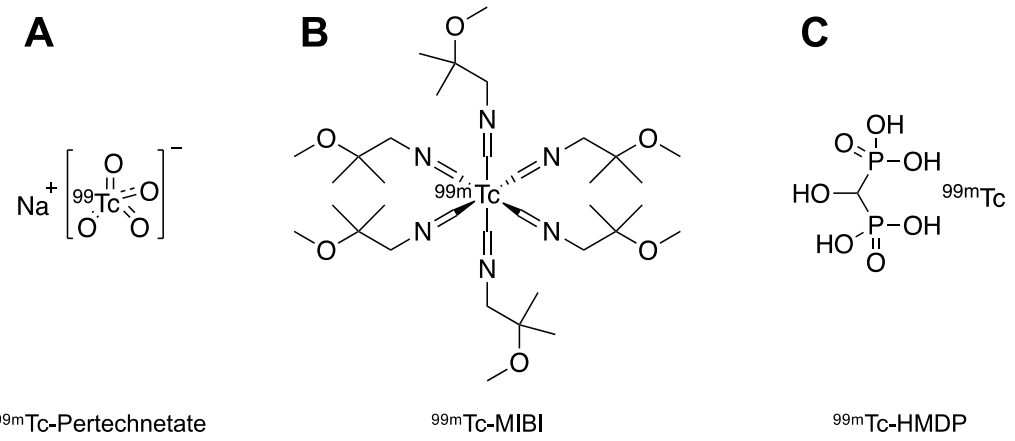


***Figure 3*** *Structural formulas of the tracers*

***(A)*** *$^{99m}$Tc-pertechnetate is commonly used for thyroid imaging and is standard for performance measurements, (**B**) $^{99m}$Tc sesta-methoxyisobutylisonitrile ($^{99m}$Tc-MIBI) is used for myocardial scintigraphy, and (**C**) $^{99m}$Tc hydroxymethylene diphosphonate ($^{99m}$Tc-HMDP) is used for bone scintigraphy. Structural formulas were created using ChemDraw software (ChemDraw version 16.0, PerkinElmer, Inc., Waltham, MA, USA). Own illustration.*

### 1.4.3 $^{99m}$Tc-MIBI for cardiac imaging

Myocardial perfusion scintigraphy is mainly used to visualize the perfusion of the myocardium [57]. Different radiotracers are available for this examination, including $^{99m}$Tc-MIBI [24] and $^{99m}$Tc-Tetrofosmin [58]. $^{99m}$Tc-MIBI is the most widely established and was also used in this work. It consists of $^{99m}$Tc bound to six methoxyisobutylisonitrile ligands [24]. The skeletal formula is shown in ***Figure 3B***. It is lipophilic, cationic and accumulates mainly in tissues that are well-perfused, have a high mitochondrial membrane potential, and mitochondria content. This is the case in tissues with very strong metabolic activity, such as the heart. $^{99m}$Tc-MIBI is characterized by long persistence in myocardial cells after tracer uptake. A limitation is the relatively high liver uptake, which may influence image quality [59].

Myocardial perfusion imaging usually consists of two images, one at rest and one under stress, i.e., after administration of a dopamine analog or after exercise [60]. If an area of the heart has decreased tracer uptake, this indicates poor perfusion. On the one hand, if the exercise image is unremarkable, hemodynamically relevant coronary artery disease (CAD) can be ruled out. On the other hand, if it is conspicuous, the resting image helps in further differentiation. Areas with decreased uptake in both images, are most likely scars (irreversibly decreased blood flow), while the areas that show decreased

uptake only in the stress image, but not in the rest image, suffer from stress-induced ischemia (reversibly decreased blood flow).

The interpretation of the images is based on single slices of the left ventricle in three planes (short axis (SA), horizontal long axis (HLA), vertical long axis (VLA)) and with the help of so-called Polar Maps, in particular, the 17 segment model of the American Heart Association [61].

This examination, along with other functional assessments of cardiac function, such as stress electrocardiogram, stress echocardiography, dobutamine stress MRI, and myocardial perfusion MRI, is an essential component of the diagnostic workflow for CAD [62]. CAD is one of the most prevalent and economically relevant diseases. Moreover, it is a leading cause of death in Western societies [63]. At what time this examination should take place is defined by the European society of cardiology (ESC) guideline [62]. Further, the 2016 Coronary Artery Disease Reporting and Data System (CAD-RADS) may help [64]. According to the latter recommendation, functional assessment is considered in CAD-RADS 3-5, i.e., from a coronary stenosis of 50% in CT diagnosis. This applies to symptomatic and asymptomatic patients with an intermediate pretest probability of chronic coronary syndrome. Scintigraphy or SPECT examinations offer advantages over other functional tests, such as high diagnostic accuracy and well-evaluated prognostic value [65, 66]. However, it also has drawbacks. Especially in obese patients false-positive results are recorded in the inferior/anterior region. Further, false-negative results are registered in 3-vessel CAD with uniformly poor perfusion because uptake values are seen relative to surrounding tissue, and the examination is associated with radiation exposure [67-69].

In addition to myocardial perfusion, it is possible to determine left ventricular ejection fraction with $^{99m}$Tc-MIBI. Besides its approval for cardiac imaging, there are additional indications for breast cancer in unclear mammography [70] or for intraoperative localization of parathyroid tissue [71].

It should also be mentioned that $^{18}$F fluorodeoxyglucose ($^{18}$F-FDG)-PET is an alternative to SPECT examination of the heart. It has certain advantages, such as increased sensitivity, specificity, and determination of myocardial blood flow and myocardial flow reserve [72]. Nevertheless, SPECT remains by far the most commonly used nuclear medicine procedure in CAD [54].

### 1.4.4 $^{99m}$Tc-HMDP for bone mineralization imaging

Bone scintigraphy is one of the most common nuclear medicine examinations and is a highly sensitive method for benign and malignant bone changes [73]. Planar scintigraphy is able to detect altered metabolic activity in bone several weeks to months prior to the detection of a morphologic correlate by an X-ray-based procedure, and it requires relatively low radiation dose. Diagnostic accuracy has been significantly increased through SPECT as well as SPECT/CT and is mostly comparable to MRI in terms of sensitivity [74]. Tracer accumulation in bone highly depends on blood flow and osteoblast activity [75]. Since most bone lesions show increased blood flow and bone turnover, an accumulation of the tracer occurs. However, there are some limitations to consider, such as low sensitivity in osteolytic metastases or multiple myeloma, to name a few [75, 76]. An overview of the typical indications for bone SPECT and SPECT/CT is shown in ***Table 1***.

***Table 1*** *Indications for bone SPECT/CT*

| | |
|---|---|
| Oncology | - In case of abnormal planar scintigraphy to improve lesion localization<br>- Assessment of malignant or pseudomalignant lesions |
| Orthopedics | - Suspected traumatic injuries of the axial or appendicular skeleton<br>- Evaluation of painful prosthesis<br>- Assessment of lesions in the tarsal or carpal small bones, in particular after trauma<br>- Evaluation of residual pain after orthopedic surgery on the axial or peripheral skeleton |
| Rheumatology | - Assessment of the spine and sacroiliac joints in case of rheumatic disorders<br>- Diagnosis of tendinitis |
| Infectiology | - Diagnosis of infectious lesions, such as osteomyelitis and spondylodiscitis (complemented with infection imaging) |
| Others | - Suspicion of axial or peripheral osteoid osteoma<br>- Diagnosis of osteonecrosis and bone infarction<br>- Exploration of extraskeletal pathology or uptake |

*Adapted from "The EANM practice guidelines for bone scintigraphy," by Van den Wyngaert et al. [75].*

The tracers used for bone scintigraphy are usually technetium-labeled phosphate analogs. These include, for example, $^{99m}$Tc-HMDP, $^{99m}$Tc methyl diphosphonate ($^{99m}$Tc-MDP) and some more. $^{99m}$Tc-MDP and $^{99m}$Tc-HMDP are the most commonly used, with $^{99m}$Tc-HMDP having the fastest blood clearance [77]. The skeletal formula of $^{99m}$Tc-HMDP is displayed in ***Figure 3C***. Lastly, there were no significant differences between these agents regarding image quality. In this thesis, $^{99m}$Tc-HMDP [25, 26] was used for bone scintigraphy.

It should be noted that $^{18}$F sodium fluoride ($^{18}$F-NaF)-PET is also an option for bone imaging and may be an alternative when available [78, 79]. Furthermore, there are promising tracers for SPECT that are bisphosphonate-based currently under investigation for clinical practice [80, 81].

One additional application of these tracers is imaging in myocardial infarction and, especially, in amyloidosis [82]. In this context, scintigraphy with bone tracers has recently been included in the practice guidelines for heart failure, as it may help to avoid biopsy in some cases.

## 1.5 Single-photon emission computed tomography

The foundation for imaging the location of gamma emitters was the gamma camera, which was first described by Hang O. Anger in 1958; it is often referred to as the Anger camera [83]. Such a device consists of a collimator, scintillation crystals for converting gamma rays into visible light, photomultiplier tubes (PMTs), and a signal processing unit that stores the raw data. Based on the registered data, a two-dimensional (2D) image of the tracer distribution can be generated.

The technology was further developed to produce three-dimensional (3D) images. This led to the invention of the first SPECT systems around 1963 [84]. The tracer distribution in the scanned volume is measured from different angles, analogous to CT. 3D images can be created from several 2D images with the help of algorithms. Another breakthrough was the combination of a SPECT modality with CT scanners, which improved sensitivity and specificity of the examinations due to enhanced attenuation correction and morphological correlation [31]. The first designs of SPECT/CT were introduced in 1990 by Hasegawa et al. [85] and became available in the clinic around 2000 [86, 87]. Over the past two decades, single-photon emission imaging has faced many challenges, most notably some technical superiorities of PET for certain applications.

Nevertheless, SPECT/CT has been further improved, and new tracers have been introduced, resulting in a continuously increasing number of installed systems [88]. In recent years, the technological advantage of PET has been reduced, while key advantages of SPECT, such as better area coverage due to independence from a cyclotron and the potential for simultaneous imaging of multiple isotopes, remain [9]. New clinical SPECT systems are able to achieve resolutions of up to 3.00 mm for certain applications [89]. In small-animal imaging, the maximum resolution of SPECT even significantly exceeds that of PET [11, 90].

Most clinical as well as preclinical systems are still based on the principle used by Anger. However, there are different approaches and components to produce the best possible image. In the following, the individual components of a SPECT system are explained and differences between the available components are highlighted.

### 1.5.1 Collimators

The collimator is the first component that photons pass through after they leave the body, or the object being scanned. Hence, only photons from a specific direction are able to hit the detector (line of response) [43]. Like this, the direction of the radiation source can be determined. Gamma rays that do not derive from the preferred direction of the collimator are absorbed and ideally do not reach the detector at all. Typically, only about $10^{-4}$-$10^{-2}$ will pass these holes, severely limiting the system's sensitivity. To achieve this selection, the collimator must be made of dense material with corresponding permeable holes; lead or tungsten are common [91]. The required material thickness depends on the photon energy since high-energy photons penetrate the material more easily, which then may lead to interfering radiation on the detector [92].

The design of the collimator and the geometrical arrangement between the radiation source and the detector have a decisive impact on the generated image [93]. To produce a high-quality image of the target volume with clinical or scientific added value, the selection of the collimator is essential.

The different designs' advantages and disadvantages will be briefly presented in the following. An overview of some common types is shown in ***Figure 4***.

The parallel-hole collimator (***Figure 4A***) is the most widely established in the clinical field [93]. It can be used for planar scintigraphy and SPECT and involves parallel holes usually configured in a honeycomb shape. These allow only photons whose vector is perpendicular to the detector surface to hit the detector. The longer these septa and the smaller the hole diameter, the fewer the incident photons are transmitted, thus increasing

the maximum resolution and decreasing the sensitivity. If these holes are no longer aligned parallel but diverging or converging, this results in a corresponding extension or reduction of the FOV. Diverging collimators (***Figure 4B***) are used, for example, in industrial reactors where a large FOV must be scanned by a small detector [94]. They are of little importance in imaging living organisms due to their low spatial resolution. On the contrary, converging collimators (***Figure 4C***) can project a small target volume onto a larger detector and are used as so-called fan-beam or cone-beam collimators with the advantage of increased sensitivity and resolution [93]. A typical application for these collimators is brain SPECT [95-97].

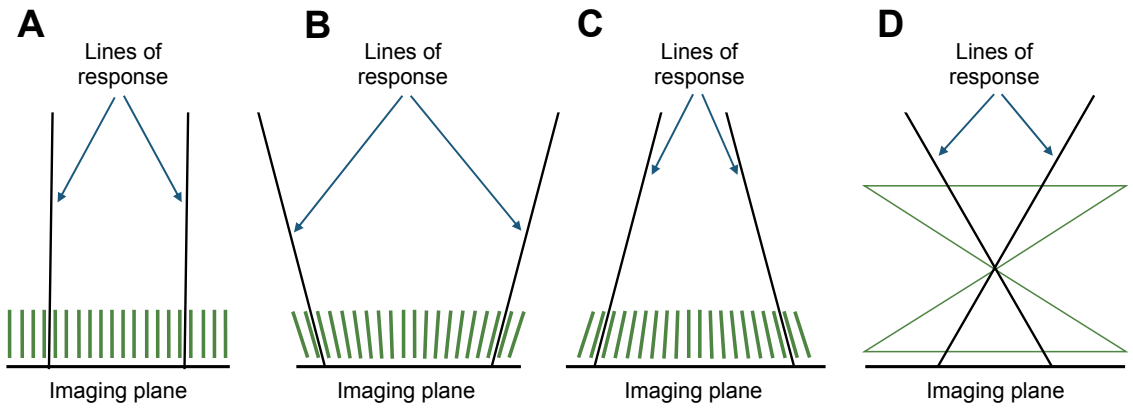


***Figure 4*** *Illustration of different collimators*

*(**A**) parallel holes, (**B**) converging holes, (**C**) diverging holes, and (**D**) a pinhole. The lines of response show possible directions in which photons could pass through the collimator. The imaging plane corresponds to the detector surface. The collimator septa are colored green. For the pinhole collimator, the green area indicates the angle of acceptance of the photons. Own illustration based on "Nuclear Medicine Physics: A Handbook for Teachers and Students" by Bailey DL et al. [43].*

Pinhole collimators (***Figure 4D***) consist of cone- or trapezoidal-shaped holes with usually a knife-edge profile [93]. These pinholes allow photons from different angles of incidence to pass through, creating an inverted projection of the radiation source on the detector. A magnifying or reducing projection can be obtained depending on the relationship between the focal length and the distance between the radiation source, pinhole, and detector. Usually, the collimator is positioned as close as possible to the radiation source to increase the resolution and sensitivity of the system. This technique is beneficial for scanning small volumes [13]. By using multiple pinholes in the form of a multi-pinhole collimator, the sensitivity can be further increased [98]. Hence, by projecting a small FOV onto a large detector, high sensitivity and high spatial resolution can be achieved. Theoretically, the maximum image quality is only limited by the number of projections,

the magnification ratio, the detector size, and the detection capacity of the detector [99]. However, overlapping projections on the detector surface are challenging, as neighboring pinholes are projected onto overlapping detector areas, and this can lead to reduced resolution and artifacts [100]. There are two approaches to address this issue. Either an attempt is made to avoid overlapping, e.g., by using shielding elements, or special sampling methods are used to minimize the adverse effects and benefit from increased sensitivity. However, no clear advantage has yet been proven for this approach [101, 102]. In addition to small-animal imaging, pinhole technology can be used clinically to image smaller organs such as the thyroid gland, individual joints, or the brain, for example [103-105].

While clinical PET might achieve better resolution and sensitivity in certain applications, the unique feature of small-animal SPECT systems with multi-pinhole collimation [11] is that they significantly exceed the spatial resolution of PET systems [106] with 0.25 mm compared to 2.00 mm. However, there are efforts to increase the resolution of small-animal PET by integrating collimators, which significantly reduces the far superior sensitivity [90]. Still, there are physical limitations restricting the theoretical maximum resolution of PET, as the positron, e.g., in the case of $^{18}F$, travels a distance of approx. 0.54 mm until annihilation [106].

There are a variety of collimators, and research continues to find the ideal solution for different applications. For high resolution small-animal studies, as performed in this thesis, the multi-pinhole SPECT seems to be the most promising approach [13].

### 1.5.2 Detectors

The purpose of the detector is to register the photons that have passed the collimator. These are then converted into an electrical signal containing information about the individual photons to reconstruct a digital image [37]. To achieve good detection efficiency, the detector must have a high intrinsic and energy resolution, as well as high count rate capability. In addition, uniformity and consistency in the measured information are essential.

The intrinsic spatial resolution, i.e., the distance up to which two photons can be distinguished on the detector surface, affects the maximum spatial resolution in the reconstructed image [37]. A good energy resolution allows to determine the photon energy as precisely as possible. The better the energy resolution, the better the photons passing the collimator unhindered can be distinguished from those that have been attenuated or scattered. With an appropriate scatter correction, the image quality can be

improved. In addition, good energy resolution enables imaging with multiple radioisotopes simultaneously since the incoming photons can be differentiated based on their specific energy [107]. The count rate capability is essential to be able to perceive as many of the incoming photons as possible [37]. If this is exceeded, the photons increasingly hit the detector without contributing to the image. This is more relevant at high count rates in PET than at low count rates in SPECT. One way to overcome this problem is to use several separate detectors.

Uniformity and temporal consistency are essential for the SPECT system to produce reliable results throughout the image and for the reproducibility of values within and between multiple images [37]. To ensure all these qualities, regular checks and maintenance are required.

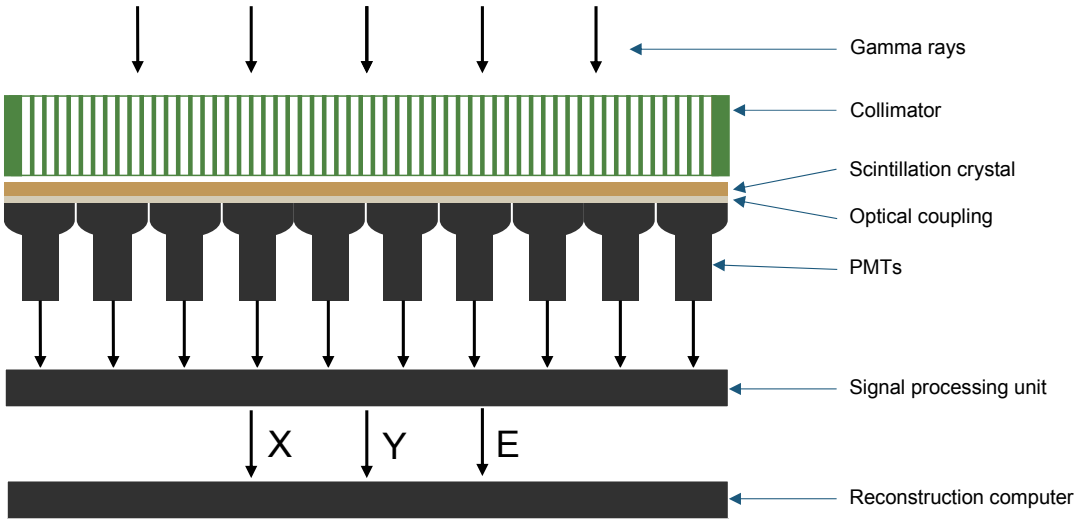


***Figure 5*** *Setup of a gamma camera*

*First, the gamma rays must pass through the collimator. Thereafter, they hit the scintillation crystal, which converts the gamma rays into visible light. The optical coupler passes this light to the photomultiplier tubes (PMTs). The light signal is transformed into a current, amplified, and transmitted to the signal processing unit. This unit calculates the location (XY) and energy (E) of the gamma rays registered at a given time. Based on this information, a digital image can be created on the reconstruction computer. Own illustration based on "Nuclear Medicine Physics: A Handbook for Teachers and Students" by Bailey DL et al. [43].*

The Anger camera (***Figure 5***) is the most widely used detector system, and part of the SPECT investigated in this work. It consists of a thallium-doped sodium iodide (NaI(Tl)) scintillation crystal connected to an optical coupler and PMTs, connected to a pulse processing unit, and an acquisition computer [83]. NaI(Tl) crystals were among the first scintillators developed by Hofstadter in 1949 [108]. Their success is due to their excellent properties in the range around 140 keV ($^{99m}$Tc): they generate an intense light signal that

allows high count rates of up to $10^5$ $s^{-1}$, and large crystals with diameters of up to 80 cm can be produced [37]. The PMTs' task is to convert the light into an electrical current. Followed by a subsequent amplification, a measurable signal is created. The total signal over all PMTs gives information about the photon energy. Further, the distribution of the signals between PMTs provides information about the location where the photons interact with the detector.

In addition to NaI(Tl), there have been numerous attempts to develop alternative scintillation crystals such as thallium-doped cesium iodide (CsI(Tl)) and several others, but these have not yet gained widespread use [109, 110].

Another type of detector gaining popularity is based on semiconductors. These allow to convert incoming photons directly into an electrical signal without the need of PMTs [49]. This leads to higher sensitivity, better energy resolution, intrinsic spatial resolution, and a reduction in scattered photons. In this regard, cadmium-zinc telluride (CZT) detectors have proven to be particularly useful. Recent advancements improved some SPECT examinations, and a reduction in scan time and radiation dose were made possible [111, 112]. The technology is already clinically well established for cardiac SPECT and is also increasingly applied for whole-body SPECT [113-117].

### 1.5.3 Image reconstruction

One of the simplest and oldest reconstruction methods is the filtered back projection (FBP) [118]. This was predominant for a long time due to the reconstruction speed with limited computing power and is still common, especially in computed tomography. How this works is briefly explained in the following:

The projection measured on the detector corresponds to the Radon transform of the tracer distribution on a straight line through the scanned object. From this one-dimensional information, a sinogram can be created by using multiple projections from different angles that, when backprojected, produce a blurred version of the scanned object. This can be imagined as drawing all these measured values on top of each other as straight lines from the corresponding detection angles in the scanned space. The blurring results from the incompleteness of the information, since only the direction and the total number of counts from that direction can be considered. To reduce this blurring, so-called high-pass filters are applied. The associated increase in image noise can be encountered by using additional low-pass filters. These filters work by changing the corresponding values for high and low frequencies in the Fourier space of each line in the sinogram, which requires a Fourier transform and an inverse Fourier transform [119].

This results in a trade-off between contrast, noise, and resolution. Furthermore, the outcome depends on the number of projections considered. The resulting 2D images can then be assembled into the 3D SPECT image.

In nuclear medicine, FBP has been replaced by iterative reconstruction algorithms to a large extent, with maximum likelihood expectation maximization (MLEM)-based methods being the most relevant [120, 121]. The iterative algorithms use forward projections in the sense of an estimate (Monte-Carlo simulation). The estimated projections are then compared to the measured projections and adjusted accordingly. The different algorithms vary in how the projections are compared and how this comparison is used in the correction for the following iteration. The first estimate is usually made randomly or by FBP and then repeated with the adjusted estimates for a given number of iterations. A key advantage of iterative methods is that they can consider the system as imperfect and thus account for scattered and attenuated photons, for example. The special feature of the MLEM algorithm is that it takes into account natural variations in radioactive decay using the so-called Poisson equation and thus gives an estimate for the tracer distribution, which maximizes the probability of generating the measured sinogram. Accordingly, each iteration consists of two steps: first, calculating the probabilities for any reconstructions based on the measured data, and second, identifying the image with the highest likelihood of generating the measured data. At each iteration, a current estimate of the image is available. A model that can account for factors such as attenuation, scattering, and application or system-specific properties is then used to simulate what the projections of this current estimate should look like. This is enabled by the system matrix, which describes for different scenarios the probabilities that photons, originating from specific voxels, hit the detector at certain positions. These are then compared to the measured projections.

The comparison changes the current estimate and creates an updated estimate for the next iteration. This process is repeated up to several hundred times, and as the number of iterations increases, the accuracy of the estimate is improved, although it should be noted that image noise builds up simultaneously. Since reconstruction with MLEM requires a lot of time and computing power, there have been continuous efforts to speed up the algorithm without degrading the result. The ordered-subsets expectation maximization (OSEM) algorithm and its further enhancements have been particularly successful [122]. The projections are divided into subsets, which go through the MLEM algorithm separately to speed up the reconstruction process [123].

In recent years there have been some further developments of the OSEM algorithm, especially for multi-pinhole SPECT as used in this work. These and their unique features are presented in the following.

In multi-pinhole SPECT, Branderhorst et al. [124] noted an increasing deviation of results with a rising number of subsets in OSEM reconstructions compared with MLEM. Reconstruction time and quality could be improved by dividing the reconstruction into subsets consisting of multiple pixels distributed over all projections rather than multiple projections from different angles.

A further adjustment was made because a high number of subsets can lead to increased image noise, especially in regions with low activity. This can lead to improper cancelation of activity, while a low number of subsets leads to a long reconstruction time, especially in highly active regions. Vaissier et al. [125] developed the count-regulated ordered-subsets expectation maximization (CR-OSEM), which uses different amounts of subsets depending on the estimated activity in an area.

An additional speed-up could be achieved with SROSEM, since with CR-OSEM the reconstruction of the areas with low activity still takes a lot of time due to the use of few subsets. With SROSEM, the number of subsets used no longer depends on the expected activity, but on how similar the predicted activity would be if the subset distribution is changed [21]. In this way, the reconstruction process could be further accelerated without losing image quality compared to the gold standard MLEM. This algorithm allows the user-friendly application of constant reconstruction parameters for a wide range of count levels in combination with a post-reconstruction filter [21]. Therefore, all images in this work were reconstructed using the SROSEM algorithm.

## 1.6 Performance evaluation and image quality

All of the hardware and software components presented in the sections above affect the system's overall performance, i.e., how well the scanner generates an accurate picture of the actual activity distribution in the scan volume in various scenarios. Standardized protocols for measuring the performance of gamma cameras and SPECT systems are published by the National Electrical Manufacturers Association (NEMA) [56, 126].

These contain instructions for measuring the performance of SPECT systems. Unfortunately, there is no dedicated small-animal or multi-pinhole SPECT protocol, and the transfer is not straightforward. The parameters measured include, in particular, spatial resolution, uniformity and sensitivity. Osborne et al. [127] and Mannheim et al. [128] have highlighted the importance of regular quality control and standardized

performance measurement of small-animal imaging equipment. The performance parameters theoretically achievable by a system, are specified by the manufacturer and defined by the hardware and software used. This varies significantly between scanners from different manufacturers. Regularly performed quality controls are necessary to ensure the consistency of results.

In this work, I have focused not only on the performance parameters but also on the image quality achieved, in order to show what kind of results can realistically be obtained with the overall system examined. Two approaches can be distinguished when evaluating image quality: firstly subjective image quality, which is based on the judgment of experts, and secondly objective image quality, which is calculated using algorithms [129].

Subjective quality assessment is considered the gold standard, because in most applications, humans are the recipients of the image and judge it according to their subjective image impressions [130]. In some cases, the assessments between readers may differ significantly, so more than one observer is required. Besides a sufficiently large group, a standardized procedure is also necessary, for example the use of a standardized rating scale [131].

A simple and common approach to determining objective image quality is calculating the contrast-to-noise ratio (CNR). Even if only some aspects of the image quality are captured compared to the subjective assessment, the CNR is an essential and versatile parameter. In addition, there are efforts to simulate the subjective image impression with more complex algorithms, but a standard has yet to be established [129].

In this thesis, image quality was evaluated based on a visual image quality assessment by professional readers and a contrast-to-noise analysis.

# 2 Objectives of the thesis

Small-animal SPECT is an essential modality for basic and translational research. Innovations in recent years have led to high-resolution imaging in rodents with sufficient sensitivity. Looking at mice, resolutions of less than one millimeter have been achieved. In rats, the performance of these systems is less well studied, although rat models have many advantages and play a crucial role in preclinical research. Therefore, it was aimed to establish a basis for rat SPECT imaging for upcoming projects with the following objectives:

1. What is the performance of the U-SPECT$^5$/CT E-Class with two stationary detectors, a dedicated rat multi-pinhole collimator, and a new reconstruction algorithm?

2. What image quality can be achieved in phantom scans, and how is it related to activity concentration and post-filtering?

3. Implement a CNR assessment using hot-rod phantoms as an objective measure for image quality.

4. What image quality and resolution can realistically be achieved in in vivo studies in rats using cardiac and bone SPECT?

5. Implement a CNR assessment method for in vivo scans as an objective measure of image quality.

6. Image quality assessment based on subjective ratings from professional readers.

7. To determine the role of SPECT in radionuclide imaging in rats by evaluating the results and comparing them with the existing literature.

# 3 Material and methods

## 3.1 System description

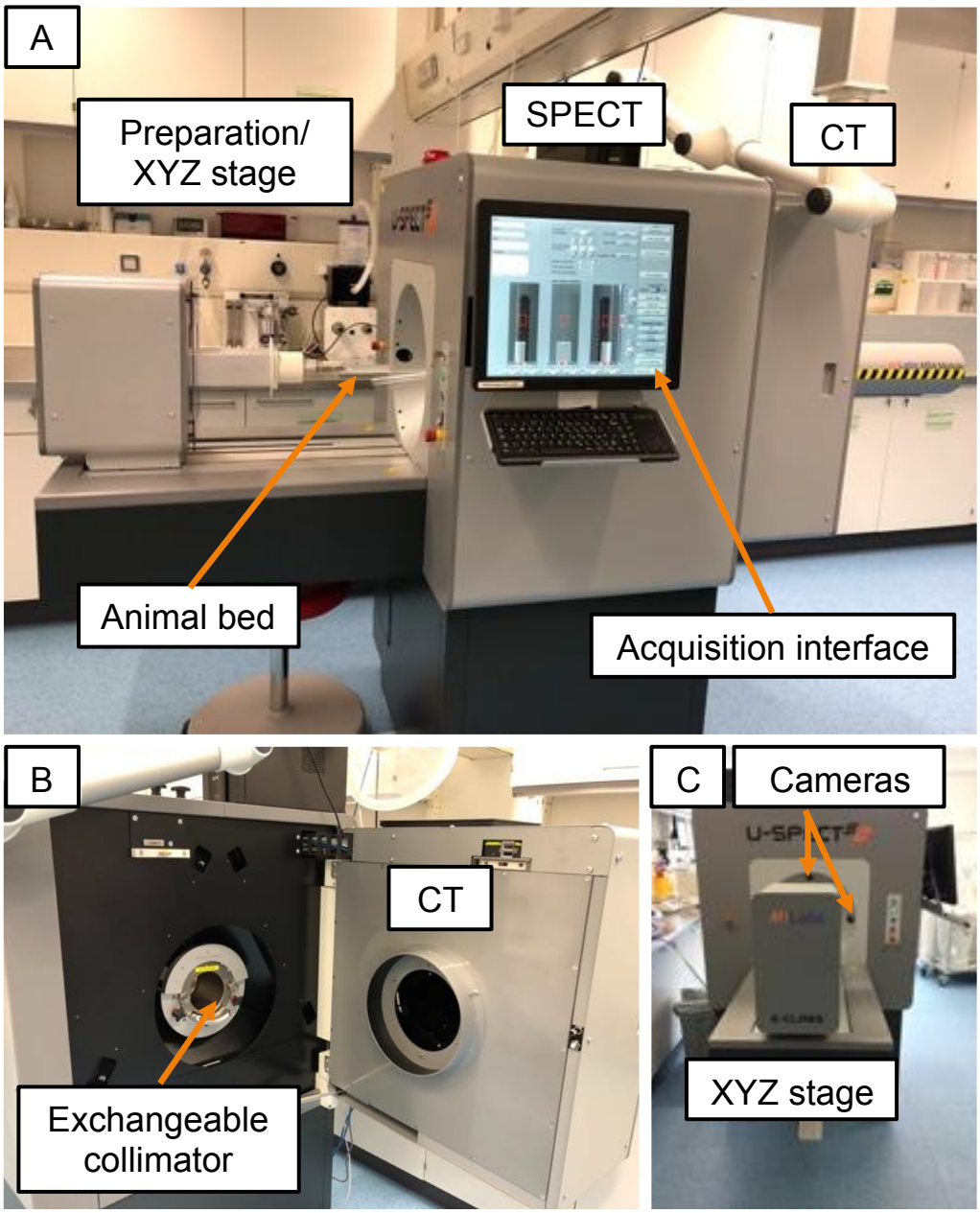


***Figure 6*** *Photos of the U-SPECT$^5$/CT E-Class*

*(**A**) shows a side view that allows the different areas to be identified: on the left the preparation area with the XYZ stage is situated to which the animal bed is attached. In the center is the SPECT unit with the acquisition user interface mounted on the outside, and on the right is the CT unit. (**B**) shows the U-SPECT$^5$/CT E-Class opened from the back. This opening between SPECT and CT component is necessary to exchange the collimator. (**C**) shows the front view. Here, the orange arrows point to two of the three optical cameras that are used to define the scan volume.*

The system investigated in this work is the U-SPECT$^5$/CT E-Class from MILabs (MILabs B.V., Utrecht, The Netherlands): A SPECT/CT developed for preclinical research and suitable for the examination of small- to medium-sized animals. For example, mice, rats, or rabbits can be examined with appropriate animal beds and collimators. Photos of the system are shown in ***Figure 6***. The design is essentially the same as the previous models U-SPECT-I, U-SPECT-II, and U-SPECT$^+$ [11, 16, 132].

The system's setup is split into three sections: a preparation section, a SPECT section, and a CT section.

The animal bed is mounted on the XYZ stage in the preparation section. This robot arm can move the animal bed in all three axes using translational movements, with a movement accuracy of 0.02 mm as specified by the manufacturer [133]. The animal or phantom is positioned in the animal bed, which in this thesis corresponds to the special rat bed made of poly(methyl methacrylate) (PMMA). Three optical cameras are aligned with the animal bed so that they can be used to perform a position check and to define the scan volume before the acquisition.

The SPECT section contains the collimator in its center. This collimator is interchangeable and is permanently aligned in the center of the detectors by a corresponding mounting device at the gantry. A construction scheme is shown in ***Figure 7***.

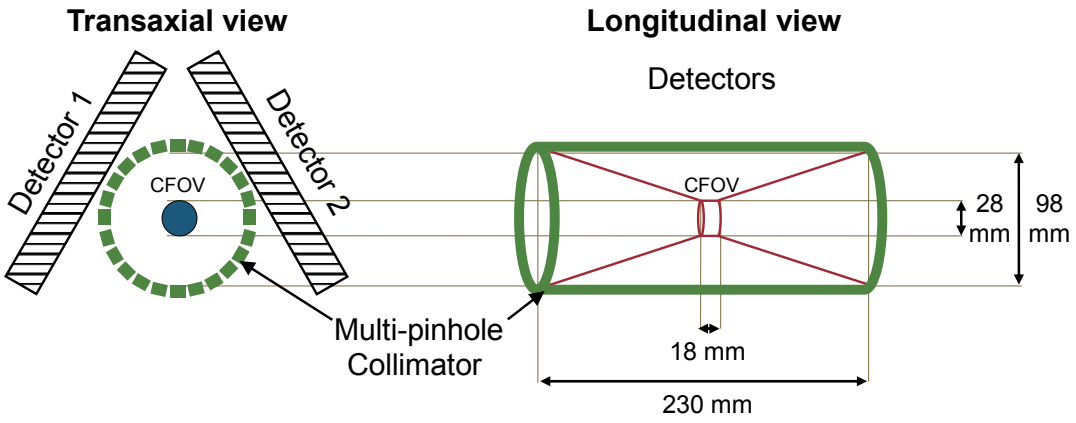


***Figure 7*** *Construction scheme of the SPECT section*

*The two detectors with a 472 mm x 595 mm detection area contain a 9.5 mm thick NaI(Tl) scintillation crystal. The ultra-high resolution rat/mouse (UHR-RM) collimator has an inner diameter of 98 mm, and the 75 pinholes arranged in five rows result in a central field of view of 18 mm in length and 28 mm in diameter. The total length of the target volume can be up to 230 mm. Adapted from "Capabilities of multi-pinhole SPECT with two stationary detectors for in vivo rat imaging," by Janssen JP et al. [27].*

The collimator used here is an ultra-high resolution rat/mouse collimator (UHR-RM), which consists of a tungsten cylinder with five rows of 15 pinholes, each with a diameter of 1.00 mm and a knife-edge profile (***Figure 8***).

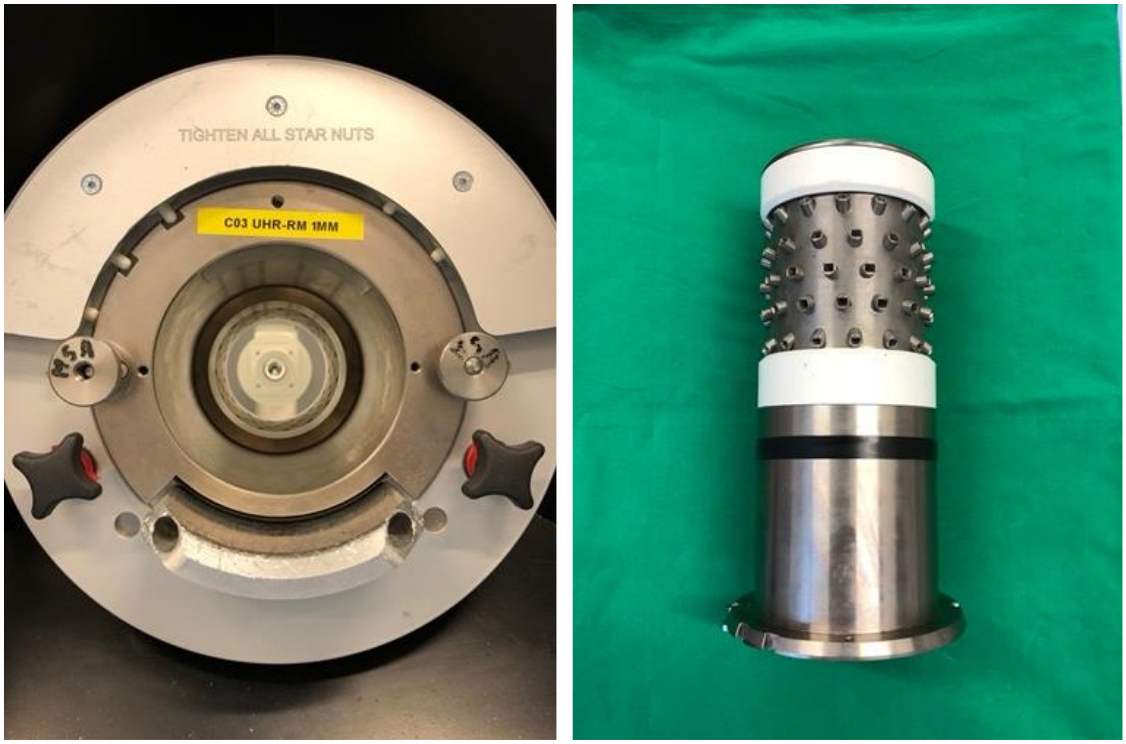


***Figure 8*** *Photos of the UHR-RM collimator*

*The left image demonstrates the rear view through the collimator mounted in the SPECT. In the center of the collimator, the XYZ stage moves the animal bed during the imaging procedure. The right image shows the dismounted collimator with the pinhole arrangement exposed.*

All these pinholes are aligned to the central field of view (CFOV), which has a diameter of 28 mm and a length of 18 mm (***Figure 7***) and is thus larger than in the respective mouse collimators (diameter: 12 mm; length: 7 mm), resulting in a reduced magnification factor of the projections while the detector surface remains unchanged. This target volume usually projects onto the three stationary detectors arranged in a triangle covering the whole circumference. In the investigated E-Class system, the lower detector was omitted so that there are only two detectors above the collimator at an angle of 60° to each other.

Consequently, only two thirds of the gamma rays passing the collimator are transmitted to the detectors. The pinholes project onto the detector surface without overlapping so that each pinhole can be assigned its unique surface section. The detectors consist of NaI(Tl) scintillation crystals with a size of 472 mm x 595 mm and a thickness of 9.5 mm

[133]. The scintillation crystals are coupled with optical grease to several PMTs that convert the optical signals into electronic signals and amplify them for output to the processing electronics. These detectors can achieve an intrinsic resolution of 3 to 4 mm and a respective energy resolution of about 10% for $^{99m}$Tc [42].
The CT section is located behind the SPECT section, so the animal bed can switch to CT directly before or after the SPECT image using the XYZ stage. The CT can be used for target volume planning, attenuation correction, or just as a micro-CT. The maximum scan volume is up to 75 mm in diameter and up to 210 mm in length. The system has a 20-65 kV X-ray source and a 1944 x 1536 x 14 bit X-ray camera [133].

### 3.1.1 Calibration and quality control

Initial calibration and quality control were performed by the manufacturer MILabs before the start of the experiments. This was followed by monthly uniformity and resolution measurements with the collimator used, as recommended by the manufacturer [133], to ensure consistent performance. A calibration factor allowing quantification of the data was determined using a point source and entered in the reconstruction software.

### 3.1.2 Data acquisition

For the scan settings, several adjustments could be made in the MILabs.Acq user interface (MILabs B.V., version 8.62) of the acquisition computer (Amplicon Liveline LTD, Brighton, UK, Model: 1538804 4917 C, with Intel® Core™ CPU i5-2400 (3.10 GHz) and 4.00 GB RAM). The target volume was defined using the respective optical cameras. The size of the target volume determines the number of bed positions (BPs) required, and the total scan time is thus calculated from the number of bed positions, the scan time per bed position (TPB), and the translation time (TT) between the individual bed positions:

$$Total\ scan\ time = BP \times TPB + (BP - 1) \times TT$$

For the scan mode, a spiral step mode was chosen because it was demonstrated that the number of necessary bed positions is reduced. Therefore the time efficiency of the performed scans is better than with multiplane trajectories [134].
The registered data of all SPECT projections were saved in list-mode format so that the energy range for the reconstruction can be defined afterwards.

### 3.1.3 Data reconstruction

Image reconstruction was performed on a dedicated workstation (Dell PowerEdge T630 server (Dell Technologies, Inc., Round Rock, Texas, USA) equipped with two Intel® Xeon® E5-2690 v4 processors (2.6 GHz each) featuring 14-core DDR4 RAM with 128 GB RDIMM memory and an M60 Nvidia® graphics card). The recorded list-mode data was processed using the dedicated reconstruction software MILabs.Rec (MILabs B.V., version 8.06).

The reconstruction algorithm was set to SROSEM with 4 iterations and 128 subsets, and a voxel size of 0.4 mm. These reconstruction settings are based on the recommendations of Vaissier et al. [21] and showed no disadvantage compared to the gold standard MLEM [120]. However, they provide a significantly faster reconstruction time [21].

For scatter correction, the triple energy window method introduced by Ogawa et al. [135] was used, whereby the photopeak window was set to 126.0 keV to 154.0 keV with a width of 20%, an upper background window was defined as 154.0 keV to 159.6 keV, and a lower background window as 120.4 keV to 126.0 keV.

The reconstructed image file was saved in the Neuroimaging Informatics Technology Initiative (NIfTI) format.

## 3.2 Postprocessing and analysis

The reconstructed images were processed using the public domain software "A medical imaging Data Examiner" (AMIDE for Mac, version 1.0.5, Stanford, CA, USA) [136]. Appropriate 3D Gaussian filters were used to reduce noise and improve image quality. Image analysis was performed using the program tools, such as drawing different regions of interest (ROIs).

The data to be analyzed was exported to Microsoft® Excel® for Mac (version 16.62, Microsoft365, Redmond, WA, USA) for further calculations and statistical analysis.

## 3.3 Tracer production

The $^{99m}$Tc was collected from the Department of Nuclear Medicine at the University Hospital of Würzburg during the days of experiments. It was available in highly concentrated form as $^{99m}$Tc-pertechnetate from the $^{99m}$Tc generator.

The $^{99m}$Tc-MIBI was also produced by the Department of Nuclear Medicine of the University Hospital of Würzburg using their standard process by reconstituting a freeze-dried MIBI-tracer-kit (Technescan™ Sestamibi, Mallinckrodt® Pharmaceuticals, Staines-

upon-Thames, England) with highly concentrated $^{99m}$Tc-pertechnetate. The mixture was stirred for 1 min, then heated in a boiling water bath for 12 min and injected after cooling to room temperature as recommended by the International Atomic Energy Association (IAEA) [137].

The bone tracer was prepared by reconstituting a freeze-dried HMDP-tracer-kit (Nihon Medi-Physics Co., Ltd., Tokyo, Japan) with highly concentrated $^{99m}$Tc-pertechnetate. The mixture was stirred for 1 min and injected after 5 min in accordance with IAEA recommendations [137].

The tracer solutions were diluted with 0.9% sodium chloride solution using pipettes and titrated to the desired activity concentration.

## 3.4 Activity measurements and decay correction

The activity of all tracer solutions was measured in the laboratory with a dose calibrator (ISOMED 2010, NUVIA Instruments GmbH, Dresden, Germany), which was checked daily as part of the quality control program.

Furthermore, the times of the dose calibrator and the SPECT system were synchronized, and the activities were decay-corrected for the elapsed time between activity measurement and scan start. The following formula was used:

$$A_s = A_0 \times e^{-\lambda t}$$

$A_s$ is the activity at the start of the scan, $A_0$ is the activity determined with the dose calibrator, $\lambda$ is the decay constant of $^{99m}$Tc ($\lambda = 3.206 \times 10^{-5}$ s$^{-1}$), and $t$ is the time interval between the activity measurement and the start of the scan.

## 3.5 Performance measurements

### 3.5.1 Sensitivity

A point source was used to determine the volume sensitivity of the system. Highly concentrated $^{99m}$Tc-pertechnetate was pipetted into the tip of an Eppendorf® Safe-Lock Tube® 1.5 ml (Eppendorf AG, Hamburg, Germany) made of polypropylene. The activity at scan start was 2.7 MBq with a volume of only 0.01 ml to avoid attenuation artifacts. This point source was then positioned in the CFOV using the XYZ stage and scanned with only one BP for a scan time of 5 min. The sensitivity describes the fraction of radioactive decay in the target volume registered by the detectors with energy in the photopeak range of the radioisotope and thus contributes to the image reconstruction.
For the calculation, the protocols of NEMA for preclinical PET systems were followed [126].
The following formula was used:

$$Sensitivity = \frac{R_i}{A_s}$$

Where $R_i$ is the detected photopeak counts per second and $A_s$ is the decay corrected activity of the point source at scan start. As recommended, more than 100,000 counts were registered during the measurement to minimize statistical variability.

### 3.5.2 Maximum resolution

To determine the maximum spatial resolution, a mini-Derenzo hot-rod phantom was used (Model 850.500, Vanderwilt Techniques B.V., Boxtel, The Netherlands). The phantom consists of a cylindrical container with a 12 mm thick and 24 mm diameter disk inside. This disk can be divided into six sectors containing holes with diameters of 1.50 mm, 1.20 mm, 1.00 mm, 0.90 mm, 0.80 mm, and 0.70 mm (***Figure 9***).
These holes were filled with a tracer solution containing $^{99m}$Tc-pertechnetate, 0.9% NaCl, and 5 µl blue ink (Pelikan Ink 4001® Royal Blue, *Pelikan Holding AG*, Schindellegi, Switzerland). The ink was used to verify that the boreholes were filled and that no air bubbles remained. The excess tracer solution was removed to keep the background activity low.

The activity concentration was kept high to reach the maximum resolution and was 285.2 MBq/ml at the start of the scan. The total scan time was 45 min with 9 BPs. This number of BPs was necessary to scan the entire hot-rod phantom.
The resolution was evaluated visually based on the smallest distinguishable rod size in the reconstructed image.

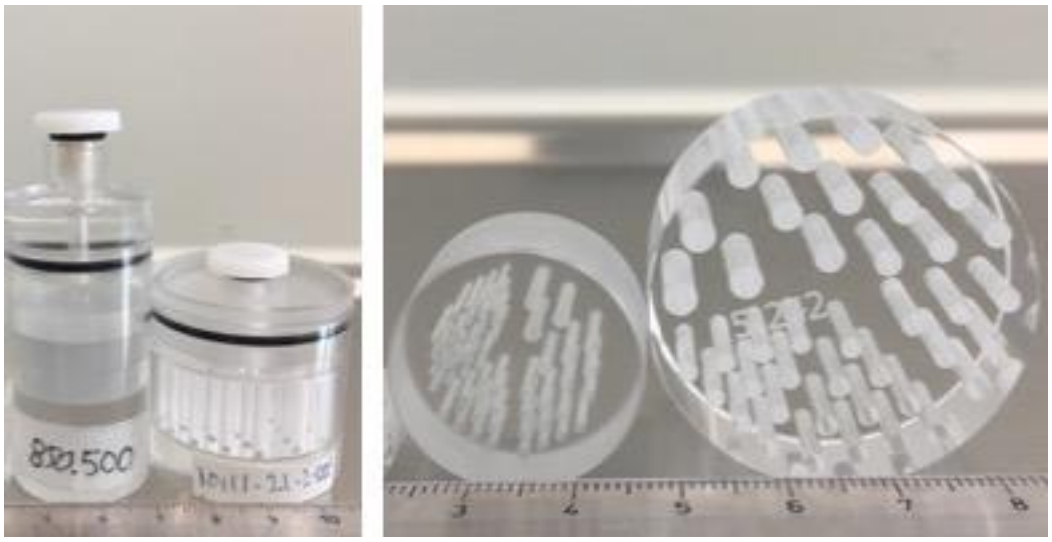

***Figure 9*** *Photos of the hot-rod phantoms*

*The two hot-rod phantoms 850.500 and 10111-21-2-008: The left picture shows the complete phantoms, including their casing, and the right picture shows only the hot-rod inlays. The phantom 850.500 was used to determine the maximum resolution and for the uniformity measurement with the inlay removed. Both phantoms were used for the contrast-to-noise ratio (CNR) analysis.*

### 3.5.3 Uniformity

To determine the uniformity, the cylindrical container of the 850.500 mini-Derenzo phantom was used. For this purpose, the inner disk with the hot-rods was removed, and the chamber was filled with 10.6 ml of $^{99m}$Tc solution. The total activity was 315.0 MBq at scan start, and the scan duration was 45 min with 9 BPs, just as for the resolution measurement. After image reconstruction, a Gaussian post-filter with the size of the maximum resolution of 1.20 mm full width at half maximum (FWHM) was applied to counteract the distortion of the values due to high image noise.
For uniformity calculation, a cylindrical ROI measuring 18 mm in diameter and 10 mm in length was placed in the center of the reconstructed image of the activity-filled phantom. System uniformity was then calculated for the UHR-RM collimator as recommended by NEMA [126] using the following formula:

$$Uniformity\ (\%) = 100 \times \frac{Max\ count - Min\ count}{Max\ count + Min\ count}$$

## 3.6 In vitro image quality

Image quality in phantom studies was evaluated using the CNR in different resolution ranges and for different count levels. The technique allows for the calculation of the CNR using hot-rod phantoms. It was initially described by Walker et al. [90].

First, high-resolution CTs of the respective phantoms were obtained at 55 kV and 0.33 mA, and these were reconstructed with a voxel size of 80 µm. Then, with their help, ROIs were defined and placed as a template over the SPECT images for evaluation (***Figure 10***).

The ROIs had a diameter of 0.9 times the respective rod diameter and a length of 6.0 mm. They were placed centrally in the individual rods and between each rod. Thus, a hot region uniformly filled with tracer and a radioactivity-free cold part in between were defined.

For this analysis, the hot-rod phantom 850.500 described above was used. In addition, another larger phantom (Model 10111-21-2-008, Vanderwilt Techniques B.V., Boxtel, The Netherlands) was used (***Figure 9***). It consists of rods measuring 3.10 mm, 2.80 mm, 2.50 mm, 2.20 mm, 2.00 mm, and 1.80 mm (***Figure 10***).

In addition to the assay of a very high activity concentration of about 300 MBq/ml, measurements in the low count range were also analyzed to represent a realistic count range for the following in vivo studies. Count ranges corresponding to activity concentrations of 1.0 MBq/ml, 0.5 MBq/ml, and 0.1 MBq/ml were chosen.

To minimize the image noise without limiting the contrast too much and thus achieve a good CNR, the reconstructed images were post-processed with a 3D Gaussian filter. The FWHM of the filter was set equal to the corresponding rod size for each resolution range investigated.

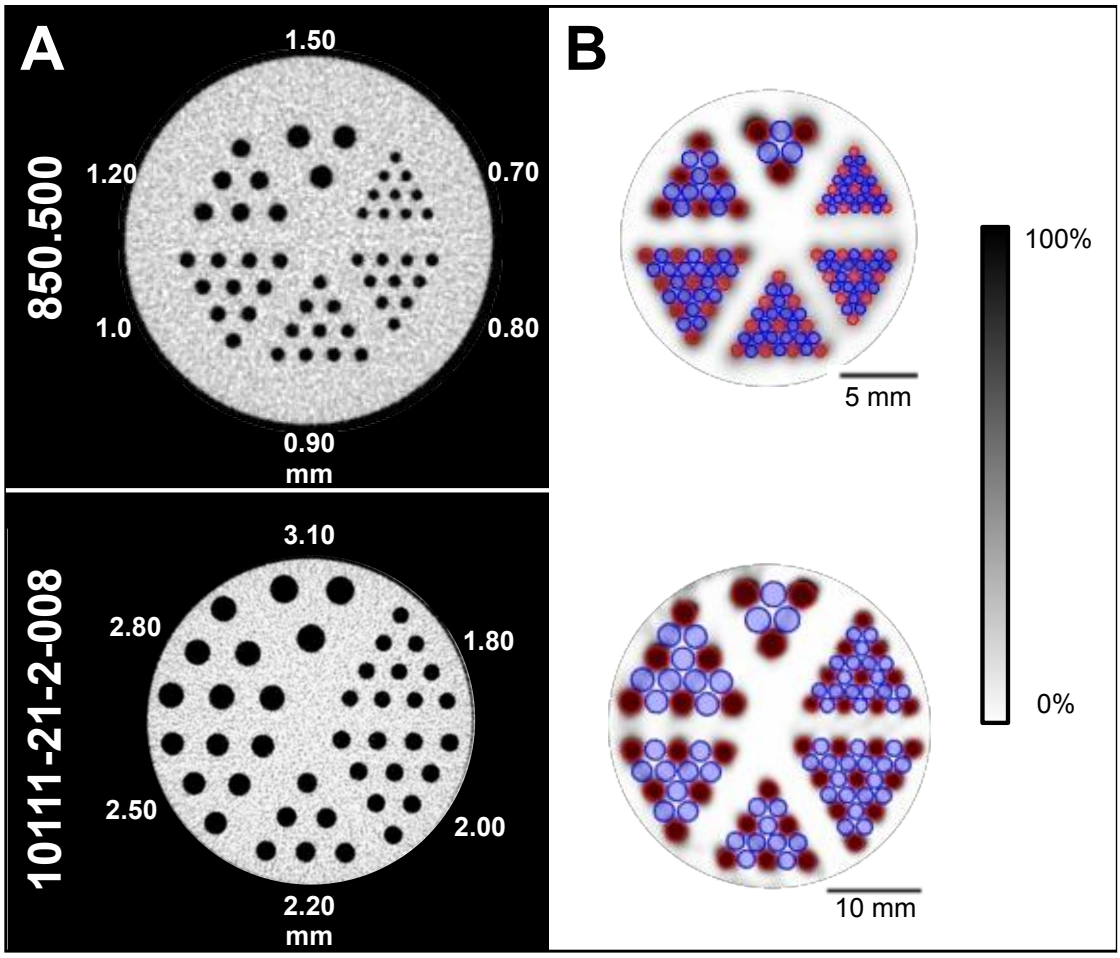


***Figure 10*** *CT images of the phantoms and CNR templates*

*(**A**) CT images in the transaxial plane of the two hot-rod phantoms 850.500 and 10111-21-2-008 with their respective rod sizes. CTs were obtained at 55 kV and 0.33 mA, these were reconstructed at 80 µm voxel size. Templates were created using these CT images to determine the contrast-to-noise ratio (CNR). (**B**) SPECT images of the corresponding phantoms with the CNR template. This consists of hot (red) regions of interest (ROIs) in the center of the rods and cold (blue) ROIs between the rods. All ROIs have a diameter of 90% of the corresponding rod diameter and a length of 6.0 mm. The SPECT images shown have a slice thickness of 6.0 mm and were acquired with 300 MBq/ml, 300 s time per bed position, 9 (850.500), and 6 (10111-21-2-008) bed positions, respectively. Adapted from "Capabilities of multi-pinhole SPECT with two stationary detectors for in vivo rat imaging," by Janssen JP et al.[27].*

The contrast $C_d$ was calculated with the following formula:

$$C_d = \frac{\overline{R_d} - \overline{B_d}}{\overline{R_d}}$$

Where $\overline{R_d}$ is the mean value of all hot ROIs and $\overline{B_d}$ is the mean value of all cold ROIs for the respective rod size $d$ under investigation.
The noise $N_d$ was calculated with the following formula:

$$N_d = \frac{\sqrt{\sigma_{R_d}^2 + \sigma_{B_d}^2}}{\overline{ROIs_d}}$$

Here, $\sigma_{R_d}$ and $\sigma_{B_d}$ are the standard deviations in hot and cold ROIs, respectively, while $\overline{ROIs_d}$ is the mean value of all ROIs of a rod size $d$, regardless of whether they are hot or cold.

These two formulas are used to calculate the CNR:

$$CNR_d = \frac{C_d}{N_d}$$

## 3.7 Animal studies

### 3.7.1 Animal preparation and general protocol

Animal experiments were approved by the responsible Commission for Animal Protection and Use (ID: 55.2.2-2532.2-801-28; "Regierung von Unterfranken" (Government of Lower Franconia), Würzburg, Germany) and performed according to the "*Guide for the Care and Use of Laboratory Animals"* by the National Research Council [138].
In this study, two healthy female Wistar rats (Charles River Laboratories, Inc., Research Models and Services, Sulzbach, Germany) were investigated. These were housed in groups under controlled and standardized conditions with a 12-hour light-dark cycle. The supply of food, water, and bedding, together with overall well-being, were monitored daily.
The rats were narcotized with 2% isoflurane (Isofluran CP®, CP-Pharma Handelsgesellschaft mbH, Burgdorf, Germany) using an induction chamber (***Figure 11***). After checking the depth of anesthesia by the between-toe reflex, the skin over the lateral tail vein was disinfected with Cutasept® F (BODE Chemie GmbH, Hamburg, Germany) for 1 min. The correct position in the vein of the 25 G cannula (Sterican® 25 G 0.50 x

40 mm, B. Braun SE, Melsungen, Germany) was tested by an initial injection of 0.1 ml NaCl 0.9%. Tracer injection as a bolus via the tail vein was then performed without complications or edema using a 1-ml syringe without residual volume (Dispomed® GmbH & Co. KG, Gelnhausen, Germany). To ensure that the administered doses were determined correctly, the activity of the syringes filled with the tracers was measured in the dose calibrator before and after the tracer injection. Further details on the bone and cardiac scan imaging protocols are provided in the following sections. At the end of each experiment, the respective rat was euthanized by decapitation.

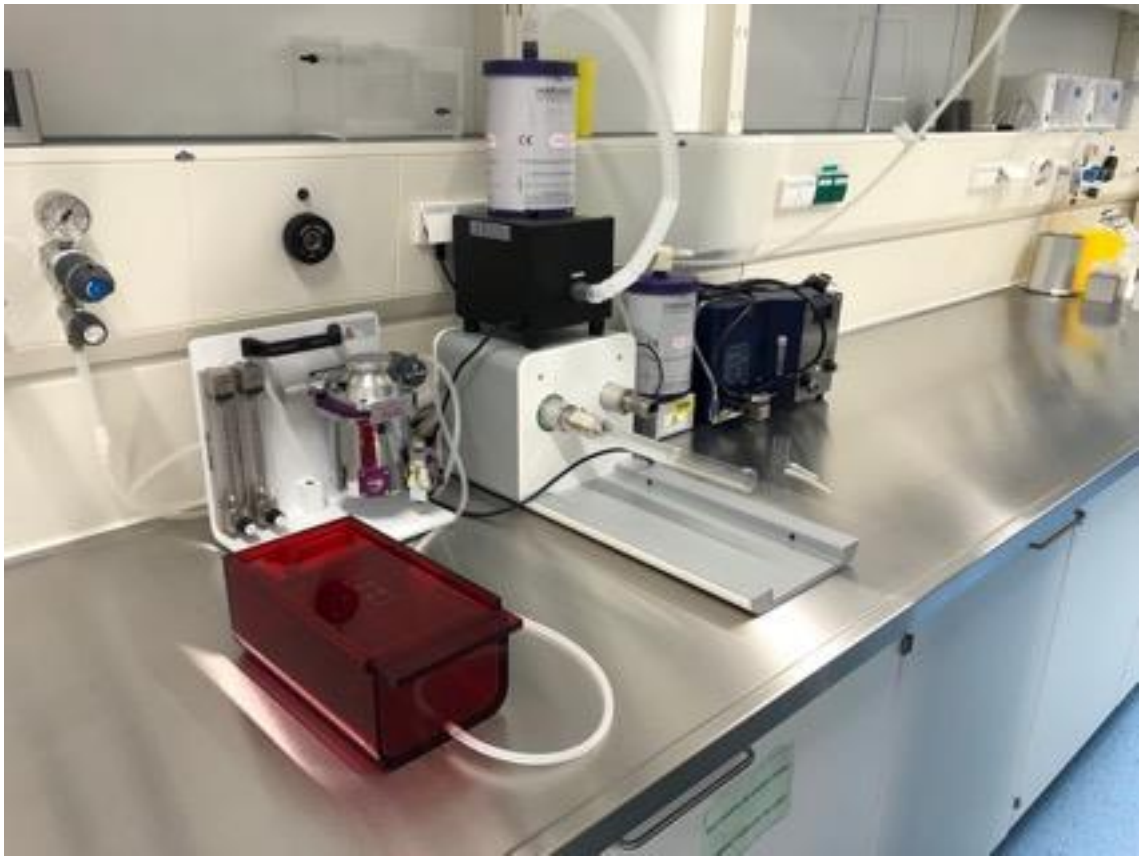

***Figure 11*** *Animal preparation area*

*The red box in the foreground serves as an induction chamber, which is connected to the vaporizer located there behind. The vaporizer is filled with isoflurane and connected to the oxygen supply in the wall. On the right is a SPECT/CT system preparation device in which the animal can be placed in the designated animal bed.*

### 3.7.2 $^{99m}$Tc-MIBI for cardiac imaging in rodents

For the cardiac tracer study, a rat weighing 231.5 g was selected. 468.73 MBq/kg of $^{99m}$Tc-MIBI was injected via tail vein. After injection, this rat was reawakened, and in

order to ensure adequate distribution of the tracer, the experiment was not continued until 25 min had elapsed [139]. Then, under inhalation anesthesia with 2.0% isoflurane at an $O_2$ flow of 1.5 l $O_2$/min, the rat was positioned on the heating mat in the dedicated rat bed with its nose in a tube connected to the vaporizer. The bed was mounted to the XYZ stage, and the target volume was set via the user interface using optical cameras. A whole-body scan was performed, so the target volume was set using the optical cameras. A total of 40 BPs were required to scan the entire body. The total length of the examination was 60 min consisting of six 10-minute frames with 15 s scan TPB.

For CNR analysis, three box-shaped ROIs with a size of 4.0 mm x 0.8 mm x 2.0 mm were placed on the hot regions of the left ventricular wall, and three additional ROIs, each of which had a distance of 4.0 mm from the corresponding hot regions, were set on the cold background (***Figure 12***).

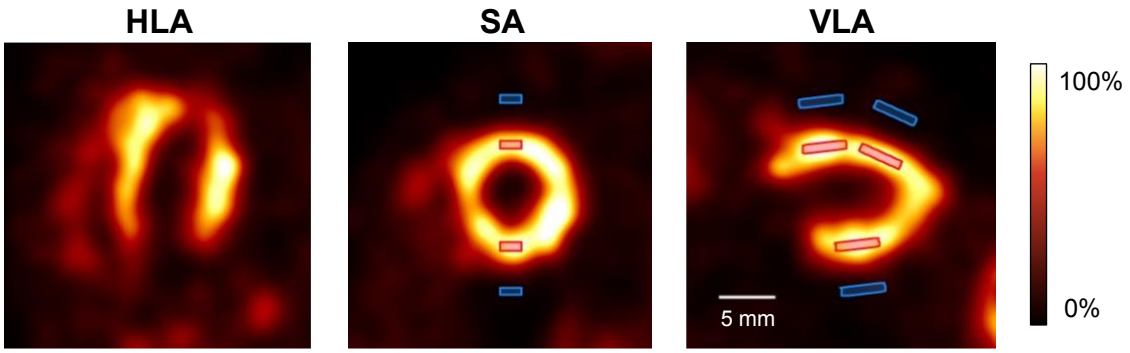


***Figure 12*** *Myocardial perfusion SPECT CNR template*

*$^{99m}$Tc-MIBI-SPECT images of a healthy rat in horizontal long axis, short axis and vertical long axis views. Images were cropped and rotated from a whole-body scan. In vivo contrast-to-noise ratio analysis for the cardiac scan was performed using hot regions of interest (ROIs) (red) in the left ventricular wall and cold ROIs (blue) in the background area next to it, each with a size of 4.0 x 0.8 x 2.0 mm$^3$. The rat was injected with 468.73 MBq/kg of $^{99m}$Tc-MIBI into the tail vein, and a 60-minute scan was performed after 25 min of tracer distribution. The reconstructed images were post-processed with a 3D Gaussian filter (FWHM = 2.2 mm) and are shown with a slice thickness of 0.4 mm. Adapted from "Capabilities of multi-pinhole SPECT with two stationary detectors for in vivo rat imaging," by Janssen JP et al. [27].*

This evaluation was performed for three different scan lengths, a short scan consisting of one 10-minute frame, a medium scan with 30 min scan time (three 10-minute frames), and a long scan with 60 min scan time (all six 10-minute frames).

In addition, these three whole-body cardiac scans were evaluated with six different filtering options. They were either unfiltered or post-processed with a 3D Gaussian filter using a FWHM of 1.2 mm, 2.2 mm, 2.8 mm, 3.5 mm, or 4.0 mm.

### 3.7.3 $^{99m}$Tc-HMDP for imaging of bone mineralization in rodents

A rat with a body weight of 217.0 g was selected for the bone tracer study. 713.64 MBq/kg of $^{99m}$Tc-HMDP was injected via tail vein. After the tracer injection, anesthesia was terminated, and the rat was placed back in the cage for 1 h to allow adequate tracer distribution.

A new inhalation anesthesia was induced with 2.0% isoflurane at an oxygen flow of 1.5 l $O_2$/min. The anesthetized animal was positioned on the rat bed analogous to the bone tracer study. The scan was focused on the lower spine and pelvis. To capture the target volume, 15 BPs were required, and the total scan time of 90 min was composed of 18 frames of 5 min length with 20 s TPB.

For the CNR analysis, box-shaped ROIs with a size of 0.8 mm x 8.0 mm x 1.2 mm were placed centrally in the right and left pelvic bones, representing the hot regions. Additionally, ROIs with the same dimensions were placed in the background on both sides, at a distance of 4.0 mm to the hot regions (***Figure 13***).

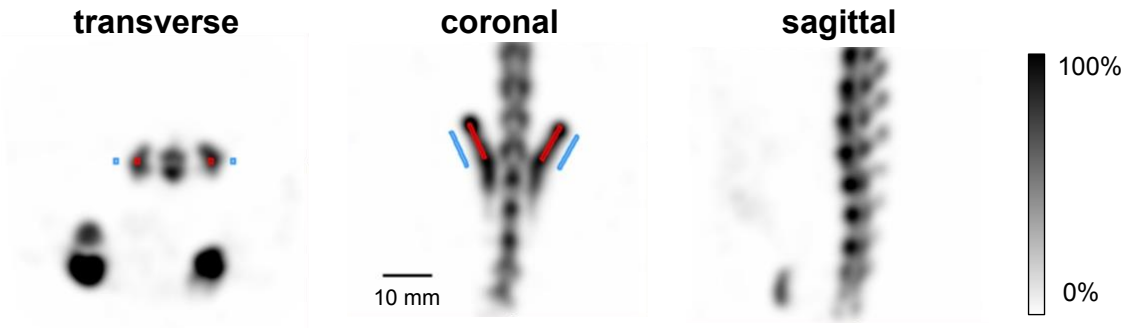


***Figure 13*** *Bone SPECT CNR template*

*$^{99m}$Tc-HMDP-SPECT images of a healthy rat's lower spine and pelvic region in transverse, coronal, and sagittal planes. In vivo CNR analysis for the focused bone scan was performed using hot regions of interest (ROIs) (red) in the pelvic bone and cold ROIs (blue) in the background region close by, each with a size of 0.8 x 8.0 x 1.2 mm$^3$. The rat was injected with 713.64 MBq/kg of $^{99m}$Tc-HMDP via the tail vein, and a 90-minute scan was performed after 1 h of tracer distribution. The reconstructed images were post-processed with a 3D Gaussian filter (FWHM = 2.2 mm) and are shown with a slice thickness of 0.4 mm. Adapted from "Capabilities of multi-pinhole SPECT with two stationary detectors for in vivo rat imaging," by Janssen JP et al.* [27].

This evaluation was performed for three different scan lengths, a short scan consisting of one 5-minute frame, a medium scan with 30 min scan time (six 5-minute frames), and a long scan (all 18 5-minute frames).

In addition, all three reconstructed scan lengths were evaluated for six different filter options. They were either unfiltered or post-processed with a 3D Gaussian filter with a FWHM of 1.2 mm, 1.8 mm, 2.2 mm, 2.8 mm, or 3.5 mm.

## 3.8 In Vivo Image Quality

### 3.8.1 Contrast-to-Noise Ratio

The CNR values for the reconstructed and post-processed animal images described in the previous sections were calculated using the same formula as for the phantom studies. However, in this case, the described ROIs in the hot and cold regions of the respective reconstructed images were used instead of the ROIs for a specific rod size.

### 3.8.2 Visual image quality assessment

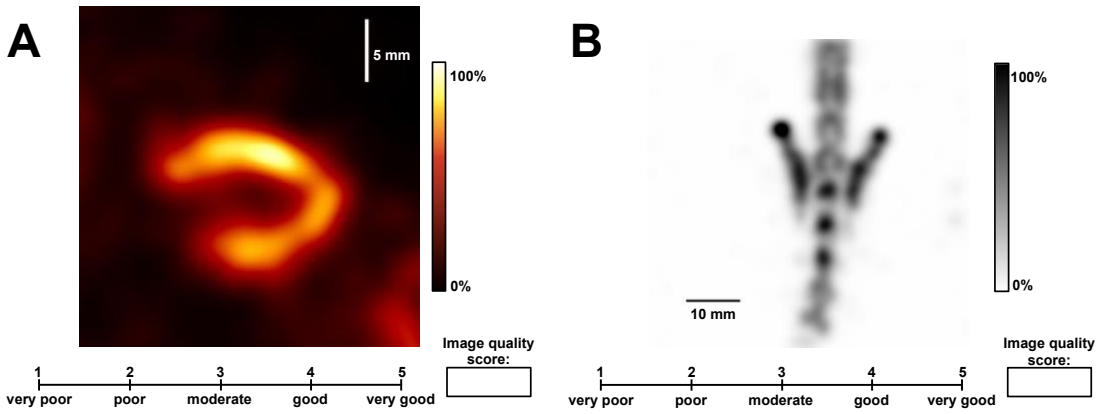


***Figure 14*** *Visual image quality assessment scheme*

*Example images of the visual image quality assessment by professional readers. (**A**) shows the vertical long axis of the rat heart with a total scan time of 10 min and a Gaussian post-filter of FWHM = 2.8 mm. (**B**) shows the focused bone scan with a total scan time of 5 min and a Gaussian post-filter of FWHM = 2.2 mm. Both images with a slice thickness of 0.4 mm are shown with their corresponding intensity and size scale. A total of 18 cardiac and 18 bone images were randomized and scored twice by each reader, blinded to scan time and post-filter. The readers entered the selected image quality score in the box at the bottom right.*

To assess subjective image impression as an indicator of image quality, the images were sent to three independent, professional readers for visual evaluation in addition to the performed CNR analysis. For this purpose, one representative image in VLA view was

selected for each cardiac image, as well as one in coronal view was chosen for each bone image (***Figure 14***). These images were duplicated for all scan lengths and all filter options, randomized, and sent to the readers. The randomization was done using an online randomization tool [140]. The readers were asked to rate the overall image quality on a five-point scale with 1 = "very poor", 2 = "poor", 3 = "moderate", 4 = "good", and 5 = "very good". They were blinded to the acquisition and post-processing protocol.

## 3.9 Statistics

Statistical analysis of the reader survey was performed using the statistic software SPSS (SPSS® Statistics Version 27 for macOS, IBM®, Armonk, New York, USA). First, the normal distribution of the continuous variables was evaluated using the Kolmogorov-Smirnov test. The categorical variables of the statistical analysis are presented as percentages, frequencies, and median values with their respective interquartile ranges (IQRs).

# 4 Results

## 4.1 Performance measurements

### 4.1.1 Sensitivity

452,907 photopeak counts could be measured in the 5-minute scan with the $^{99m}$Tc point source. This corresponds to 1509.69 cps at 2.7 MBq, thus giving a sensitivity of 567 cps/MBq (0.057%).

### 4.1.2 Resolution

Qualitative determination of maximum spatial resolution using the hot-rod phantom (***Figure 15A***) allowed sections with rod diameters of 1.50 mm and 1.20 mm to be definitively resolved. In contrast, sections with 1.00 mm and 0.90 mm rods indicated the existing structure, but not all rods could be clearly distinguished from each other. In the 0.80 mm and 0.70 mm sections, a distinction between rods and background noise was hardly or not at all possible. Consequently, the maximum resolution achieved was 1.20 mm.

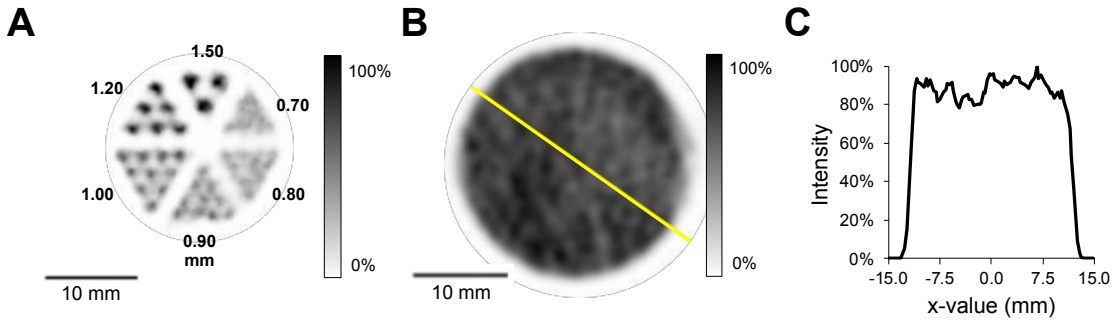


***Figure 15*** *Performance measurement results*

*(**A**) SPECT image of the hot-rod phantom (850.500). To determine maximum resolution, the phantom was filled with 300 MBq/ml $^{99m}$Tc solution and scanned for 300s time per bed position (TPB) at 9 bed positions (BPs). The smallest well distinguishable rods are 1.20 mm in diameter. (**B**) SPECT image of the phantom 850.500 without inlay, homogeneously filled with 30 MBq/ml $^{99m}$Tc solution and scanned for 300s TPB at 9 BPs. Line profile (**C**) shows respective intensity as a function of the position on the yellow line in (B). The Gaussian post-filter of the shown SPECT images corresponds to the maximum resolution of 1.20 mm. Adapted from "Capabilities of multi-pinhole SPECT with two stationary detectors for in vivo rat imaging," by Janssen JP et al. [27].*

### 4.1.3 Uniformity

The uniformity for the UHR-RM collimator with a 1.2 mm FWHM Gaussian post-filter was 55.5% based on the formula of the NEMA protocol. The maximum value in the cylindrical ROI was 39.1 MBq/ml, and the minimum value was 11.4 MBq/ml. The analyzed SPECT study and an exemplary line profile is shown in ***Figure 15B*** and ***15C***, respectively.

***Table 2*** *Performance comparison of SPECT-systems for rat imaging*

| System Name | Collimator | Sensitivity [cps/MBq] | Resolution [mm] | Uniformity [%] |
|---|---|---|---|---|
| U-SPECT$^5$/CT E-Class [27] | 75(50)-Pinhole Ø 1.00 mm | 567 | 1.20 | 55.5 |
| U-SPECT$^6$/CT E-Class [141] | 75(50)-Pinhole Ø 1.00 mm | 493 | 0.90 - 1.20 | 75.8 / 98.4 |
| U-SPECT-II [16] | 75-Pinhole Ø 1.00 mm | 700 | 0.80 | N/A |
| Inveon® SPECT [142] | 1-Pinhole Ø 1.50 mm | 40 - 70* | 1.60 - 1.80* | N/A |
| | 3-Pinhole Ø 1.20 mm | 70 - 80* | 1.20 - 1.30* | N/A |
| | 3-Pinhole Ø 1.80 mm | 140 - 180* | 2.00* | N/A |
| NanoSPECT® [143] | Multi-Pinhole Ø 1.50 mm | 998# | 1.10 | N/A |
| | Multi-Pinhole Ø 2.00 mm | 1524# | 1.50 | N/A |
| | Multi-Pinhole Ø 2.50 mm | 2229# | 1.90 | N/A |
| X-SPECT [42] | 20-Pinhole Ø 1.00 mm | 620 | 0.90 | 56.0 |
| eXplore speCZT [20] | 5-Pinhole Ø 1.00 mm | 138 | 1.20 | N/A |
| | 5-Pinhole Ø 1.50 mm | 321 | 1.50 | N/A |

**Values are an estimate based on Figure 1 in the publication by Boisson et al. [142].*

#Values may be difficult to compare since overlapping projections are used [107].

## 4.2 In vitro image quality

***Figure 16*** shows sample images of the phantoms 850.500 and 10111-21-2-008 for the examined activity concentrations. Low-activity images show increased image noise compared to high-activity images. Nevertheless, the data still feature good contrast even at low activities.

A decrease in the maximum resolution for lower activity concentrations is shown for the qualitative determination of the resolution.

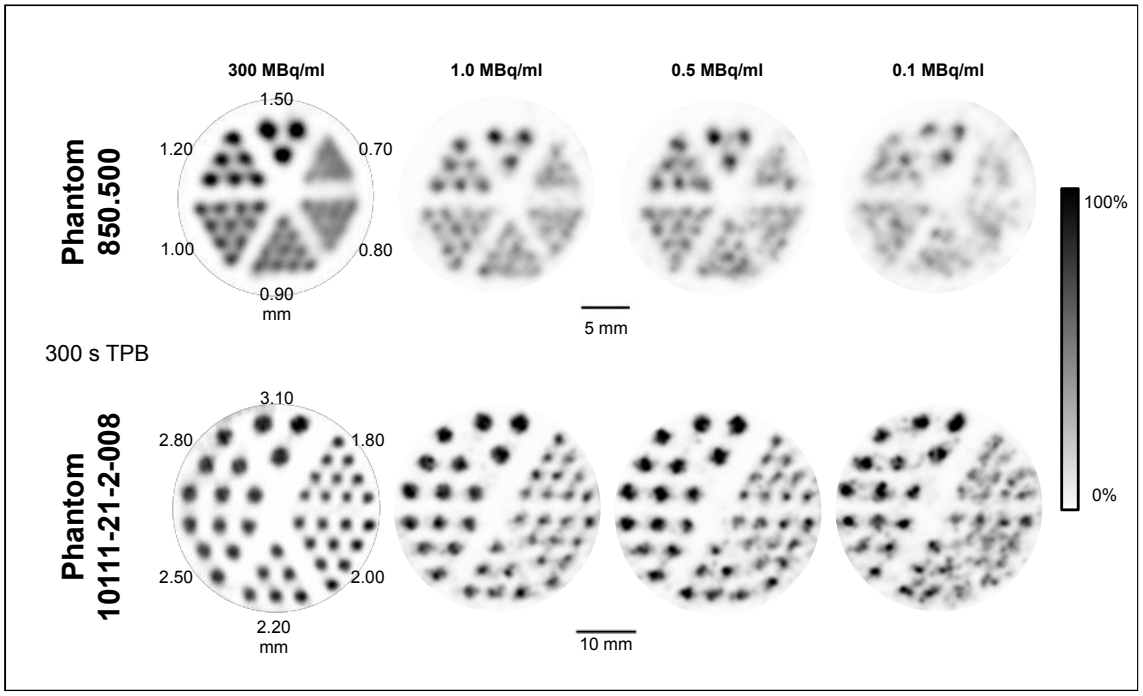


***Figure 16*** *Phantom SPECT images with different activity concentrations*

*SPECT images of hot-rod phantoms 850.500 and 10111-21-2-008 for image quality analysis. The images are shown as a transaxial plane for four different activity concentrations. One high activity measurement with 300 MBq/ml and three low activity measurements with 1.0, 0.5, and 0.1 MBq/ml. All images correspond to a time per bed position of 300s at 9 bed positions (BPs) (850.500) or 6 BPs (10111-21-2-008). Images have a slice thickness of 6.0 mm and were post-processed with a Gaussian filter of FWHM = 0.7 mm. Adapted from "Capabilities of multi-pinhole SPECT with two stationary detectors for in vivo rat imaging," by Janssen JP et al. [27].*

At the high activity concentration of 300 MBq/ml, all rods with diameters larger than the maximum resolution of 1.20 mm can be resolved, and at 1.00 mm and 0.90 mm the rod structures can be identified.

At the activity concentration of 1.0 MBq/ml, in the phantom 850.500 the rods in the sector with a diameter of 1.50 mm can still be clearly distinguished from each other. In contrast,

the resolution in the larger phantom is already somewhat limited in the sectors with ten rods of 1.80 mm and 2.00 mm in diameter.

For the activity concentration of 0.5 MBq/ml, the resolution in the corresponding sectors is even more limited. For 0.1 MBq/ml, only the sectors with rods larger than or equal to 2.50 mm can be considered distinguishable.

***Figure 17*** shows the results of the CNR analyses for the different rod sizes of the 850.500 and 10111-21-2-008 phantoms.

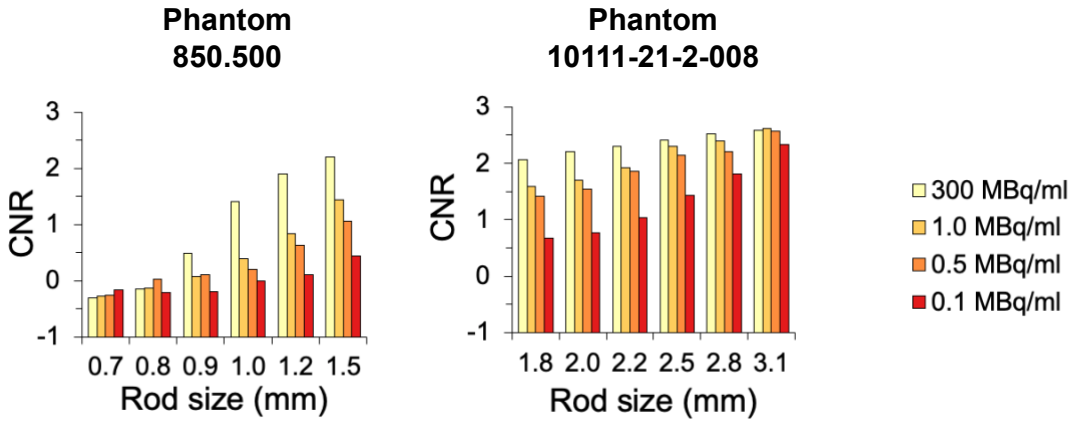


***Figure 17*** *Phantom CNR results*

*The bar charts highlight the contrast-to-noise ratio (CNR) for the different rod sizes of phantom 850.500 (0.7 - 1.5 mm) and phantom 10111-21-2-008 (1.8 -3.1 mm) for the four activity concentrations (300, 1.0, 0.5 and 0.1 MBq/ml). For calculation, each rod sector was analyzed in a separate image post-processed with a respective Gaussian post-filter (FWHM = rod size). Adapted from "Capabilities of multi-pinhole SPECT with two stationary detectors for in vivo rat imaging," by Janssen JP et al. [27].*

The CNR values were very low and partially negative for the range of rod sizes below the maximum resolution of 1.20 mm (-0.31 to 0.48). The only exception is the 300 MBq/ml measurement in the range of 1.00 mm. Here a CNR value of 1.41 was achieved.

A CNR value of 1.50 was exceeded for 300 MBq/ml at 1.20 mm, 1.0 MBq/ml at 1.80 mm, 0.5 MBq/ml at 2.00 mm, and 0.1 MBq/ml at the 2.80 mm rods.

Overall, the CNR value for all activity concentrations improved with growing rod size and correspondingly increasing post-filter. In addition, it is noticeable that the differences between the CNR values for a given rod size are equally poor in the range below the maximum resolution. Then, in the range of rod sizes from 1.00 to 3.10 mm, the CNR enhances more rapidly with high activity concentrations than with low ones. Finally, they converge again and become similarly good in the range of the largest rods (see 3.1 mm).

The difference between the CNR values of the highest activity concentration and the lowest activity concentration is most prominent in the range of the maximum resolution of 1.20 mm with a respective CNR of 1.90 for 300 MBq/ml and 0.10 for 0.1 MBq/ml.

## 4.3 In vivo image quality

### 4.3.1 $^{99m}$Tc-MIBI for cardiac imaging in rodents

***Figure 18A*** shows the $^{99m}$Tc-MIBI SPECT images of the examined healthy rat for the different scan times as maximum intensity projections (MIPs). ***Figure 18B*** depicts the heart section in the conventional three views (HLA, SA, VLA). The MIP images show a tracer distribution typical for $^{99m}$Tc-MIBI with an uptake, particularly in the myocardium, gastrointestinal organs, glands in the head region, and the urinary tract, especially the bladder [144]. No artifacts could be detected in the reconstructed images. The qualitative visual image impression shows decreasing noise and more homogeneous tracer distribution in the uptaking organs with increasing scan time and filter size. In particular, the unfiltered images show noticeable noise.

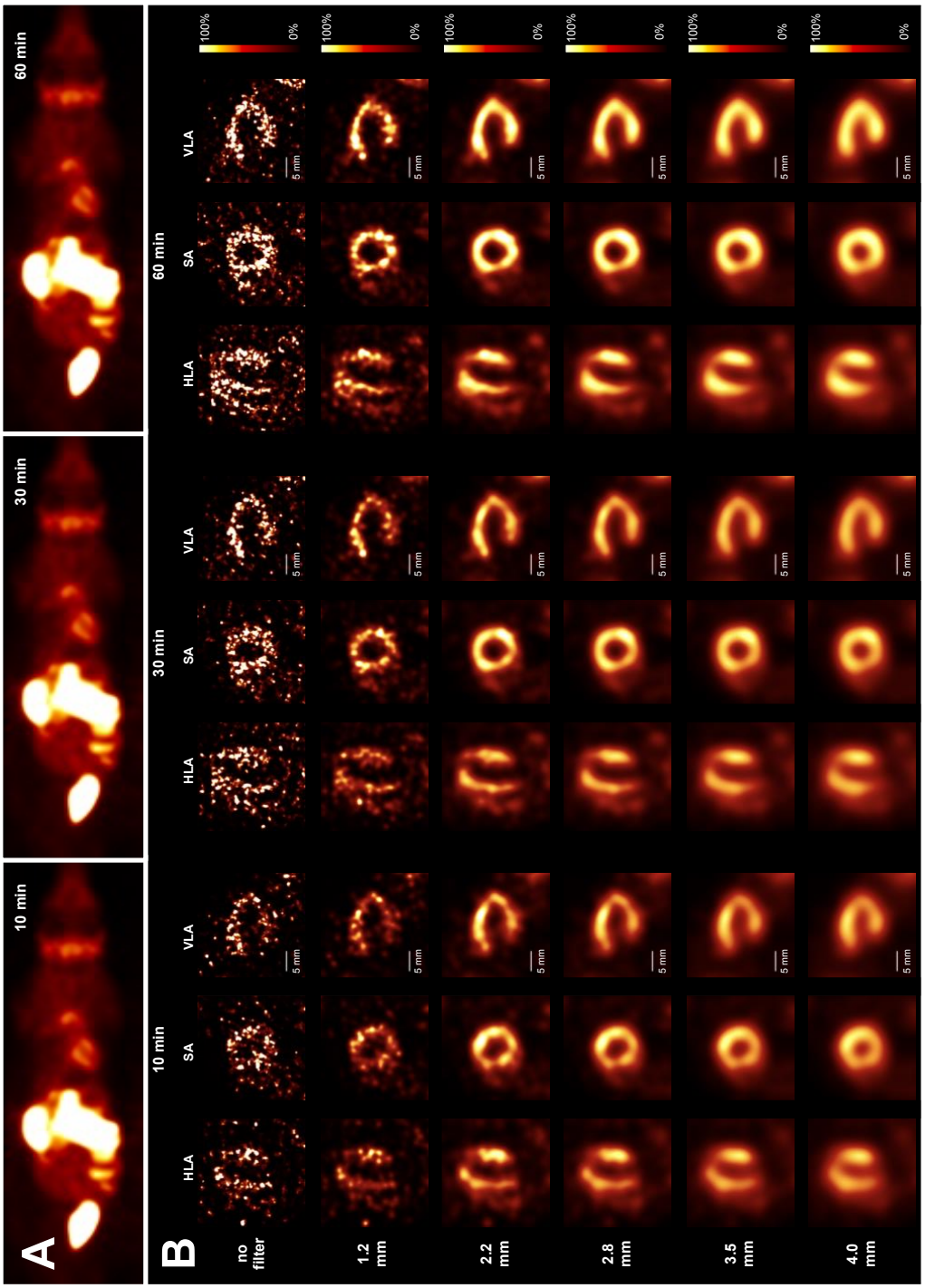


***Figure 18*** *Overview of all myocardial perfusion SPECT images*

*$^{99m}$Tc-MIBI scan of a healthy rat with an injection dose of 468.73 MBq/kg. The scan was started 25 min after tracer injection and consisted of six 10-minute frames. The reconstructed images of the first 10 min, the first 30 min, and the entire 60-minute acquisition time are illustrated. (**A**) Maximum intensity projection of the three scan lengths. (**B**) Whole-body scans cropped and rotated to show the horizontal long axis (HLA), short axis (SA), and vertical long axis (VLA). All cropped images are shown for the six Gaussian post-filter options analyzed, corresponding FWHM is indicated for each row. Adapted from "Capabilities of multi-pinhole SPECT with two stationary detectors for in vivo rat imaging," by Janssen JP et al. [27].*

The results of the CNR analysis of the left ventricular images are shown in ***Figure 19***. The unfiltered images of all scan times resulted in a very poor CNR. Increasing filter size improved CNR up to a filter size with a FWHM of 3.5 mm. In the case of the 10-minute scan, the CNR improved further with a filter size of 4.0 mm as FWHM. For the 30- and 60-minute scans, the filter with FWHM = 4.0 mm decreased CNR compared to FWHM = 3.5 mm. The increase in scan time improved the CNR for all filter sizes. Here, the peak values for the best filter option in each case rose from 6.3 for the 10-minute scan to 10.8 for the 30-minute scan and up to 12.2 for the 60-minute scan.

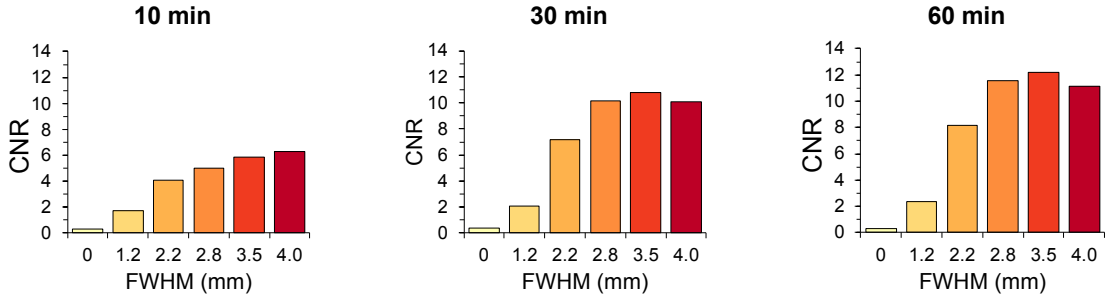


***Figure 19*** *Myocardial perfusion SPECT CNR results*

*Contrast-to-noise ratio (CNR) calculations for the myocardial perfusion SPECT images. The bar charts represent the CNR as a function of filter size for the three different scan lengths. Adapted from "Capabilities of multi-pinhole SPECT with two stationary detectors for in vivo rat imaging," by Janssen JP et al. [27].*

The selected images sent to the independent readers, as well as the corresponding survey results with image quality scores (IQ score) as a function of Gaussian filter size for the three investigated scan times are highlighted in ***Figure 20***.

Without exception, the unfiltered images received a rating of 1 = "very poor" regardless of the scan time. The best scores for the 10-minute and 30-minute scan were obtained for the images with a filter of 3.5 mm and 4.0 mm FWHM being 5.0 (IQR = 0.00) as IQ score. For the 60-minute scan, the image with the 4.0 mm filter received a slightly better IQ score of 5.0 (IQR = 0.75) compared to the image using the 3.5 mm filter having an IQ score of 4.5 (IQR = 0.5).

Scores in the range of "very poor" to "moderate" were given for the images with FWHM = 1.2 mm, in the range of "poor" to "good" for FWHM = 2.2 mm, and in the range of "moderate" to "very good" for FWHM = 2.8 mm. Overall, images obtained with post filters between 1.2 mm and 2.8 mm FWHM scored slightly better with increasing scan time.

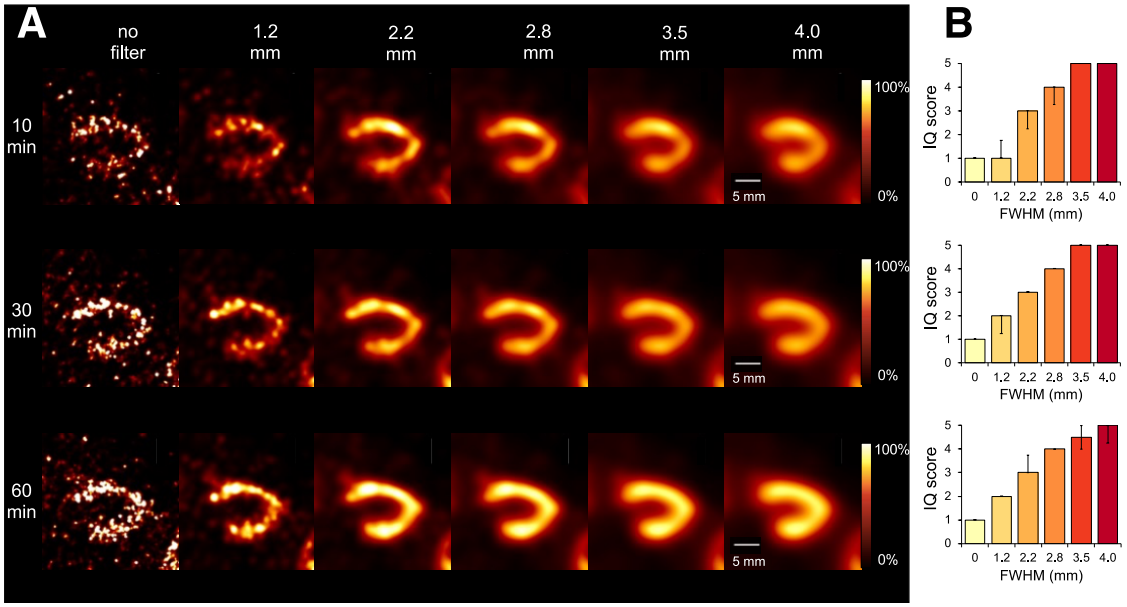


***Figure 20*** *Myocardial perfusion SPECT image quality assessment*

*(**A**) Overview of all myocardial perfusion scintigraphy images submitted to the three professional readers for evaluation. (**B**) Results of image quality assessment. Bar charts show the image quality score (IQ score) as a function of filter size for the three different scan lengths. IQ scores are shown as median values with their respective interquartile ranges. Adapted from "Capabilities of multi-pinhole SPECT with two stationary detectors for in vivo rat imaging," by Janssen JP et al. [27].*

### 4.3.2 $^{99m}$Tc-HMDP for imaging of bone mineralization in rodents

***Figure 21A*** illustrates the $^{99m}$Tc-HMDP SPECT images of the examined healthy rat for the different scan times as MIPs. ***Figure 21B*** shows the bone sections from transverse, coronal, and sagittal views. The acquired images reflect a distribution typical of $^{99m}$Tc-HMDP with sufficient tracer uptake in the bone. No artifacts were detected in the obtained data. The qualitative visual image impression shows decreasing noise and more homogeneous tracer distribution in the metabolizing organs with increasing scan time and filter size. High noise was apparent in the unfiltered images. However, high filtering, e.g., 3.5 mm FHWM, provided less detail and poorer differentiation of vertebrae and intervertebral spaces.

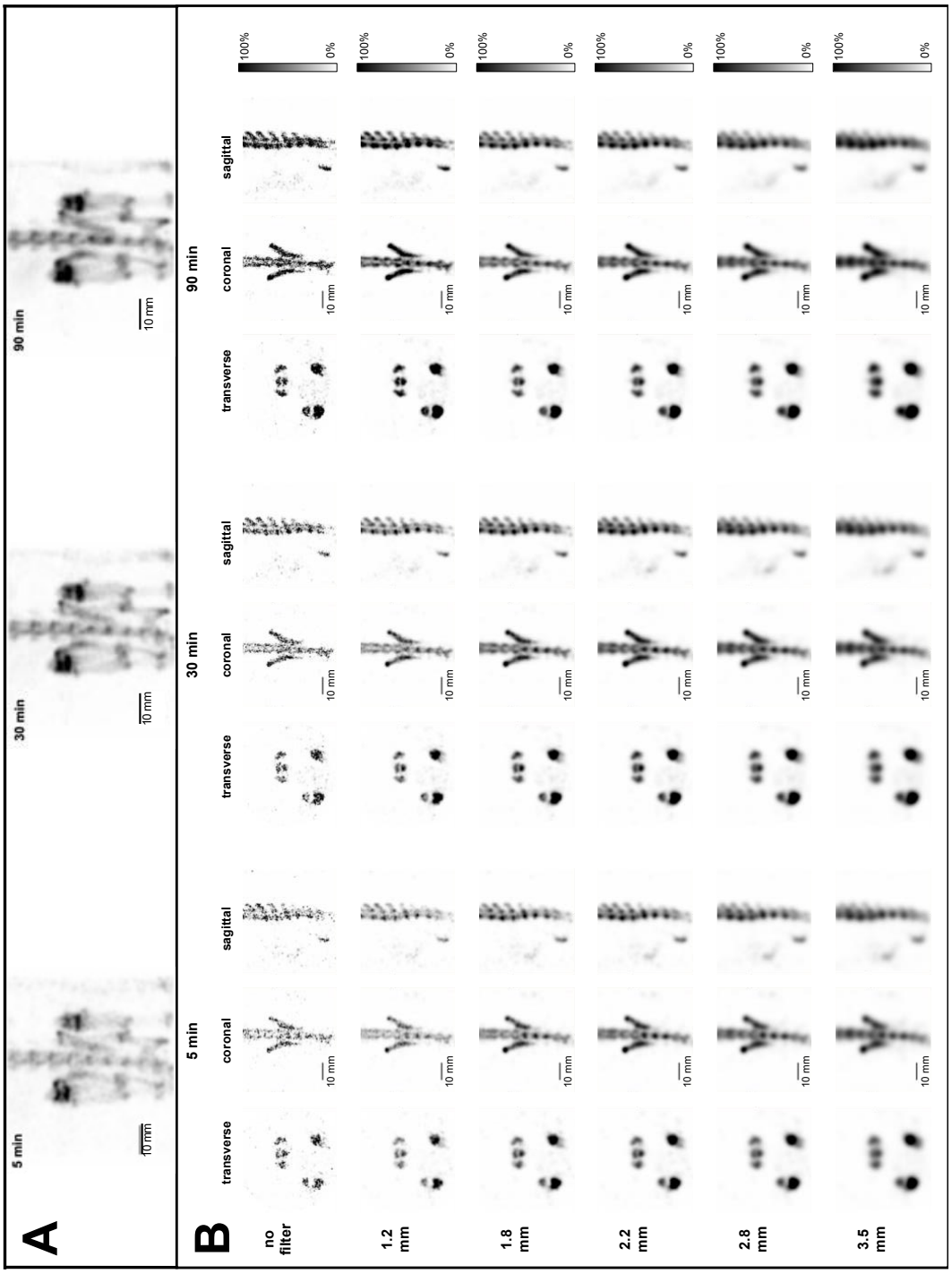


***Figure 21*** *Overview of all bone SPECT images*

*$^{99m}$Tc-HMDP scan of a healthy rat with an injection dose of 713.64 MBq/kg. The scan was started 60 min after the tracer injection and consisted of 18 5-minute frames. The reconstructed images of the first 5 min, the first 30 min, and the entire 90-minute acquisition time are shown. (**A**) Maximum intensity projection of the three scan lengths. (**B**) The images are shown in the transverse, coronal, and sagittal planes. All images in (**B**) are shown for the six Gaussian post-filter options analyzed. The sizes indicated correspond to the FWHM. Adapted from "Capabilities of multi-pinhole SPECT with two stationary detectors for in vivo rat imaging," by Janssen JP et al. [27].*

The results of CNR analysis in the pelvic bone region are shown in ***Figure 22***. The unfiltered images of all scans showed a very poor CNR. With increasing filter size and scan time, the CNR values also improved. The highest calculated CNR values for all scan lengths were achieved with a filter of 3.5 mm FWHM, reaching a CNR of 3.87 for 5 min of scan time, 4.43 for 30 min of scan time, and 4.72 for the 90-minute scan.

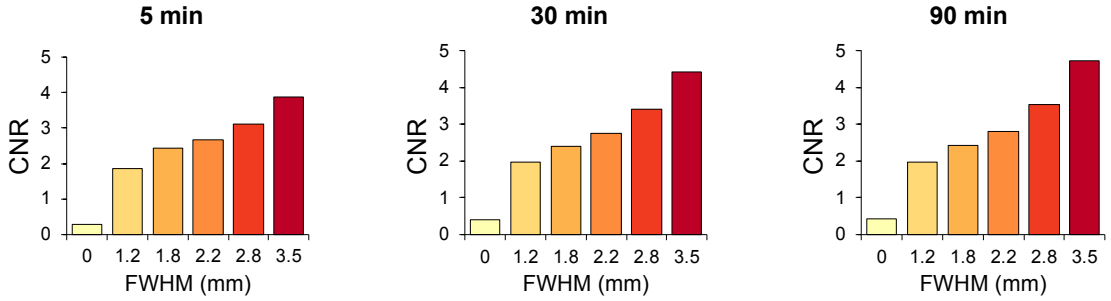


***Figure 22*** *Bone SPECT CNR results*

*Contrast-to-noise ratio (CNR) calculations for bone SPECT images. The bar charts represent the CNR as a function of filter size for the three different scan lengths. Adapted from "Capabilities of multi-pinhole SPECT with two stationary detectors for in vivo rat imaging," by Janssen JP et al. [27].*

The $^{99m}$Tc-HMDP images used for the image quality survey are shown in ***Figure 23A***. The corresponding results are shown in ***Figure 23B*** as IQ scores depending on the size of the post filter.

All readers rated all unfiltered images with the worst score of 1 = "very poor". The overall best score at 5 min of scan time was given to the image with the FWHM = 2.8 mm filter. For 30 min of scan time, the images with the 2.2 mm and 2.8 mm FWHM filters were found to be equally very good, and for 90 min of scan time, even three filter sizes with 1.8 mm, 2.2 mm, and 2.8 mm achieved equally very good results. Also, the median value of the images with 3.5 FWHM filtering for all scans was 5 = "very good"; however, there were some worse ratings, which is reflected in the larger IQR.

The scores for the images with a 1.2 mm FWHM filter ranged from "poor" to "moderate". In particular, the images filtered with 1.8 mm FWHM showed better ratings with increased scan time. Here the median value increased from 3 = "moderate" for 5 min to 4 = "good" for 30 min to 5 = "very good" for the 90-minute scan.

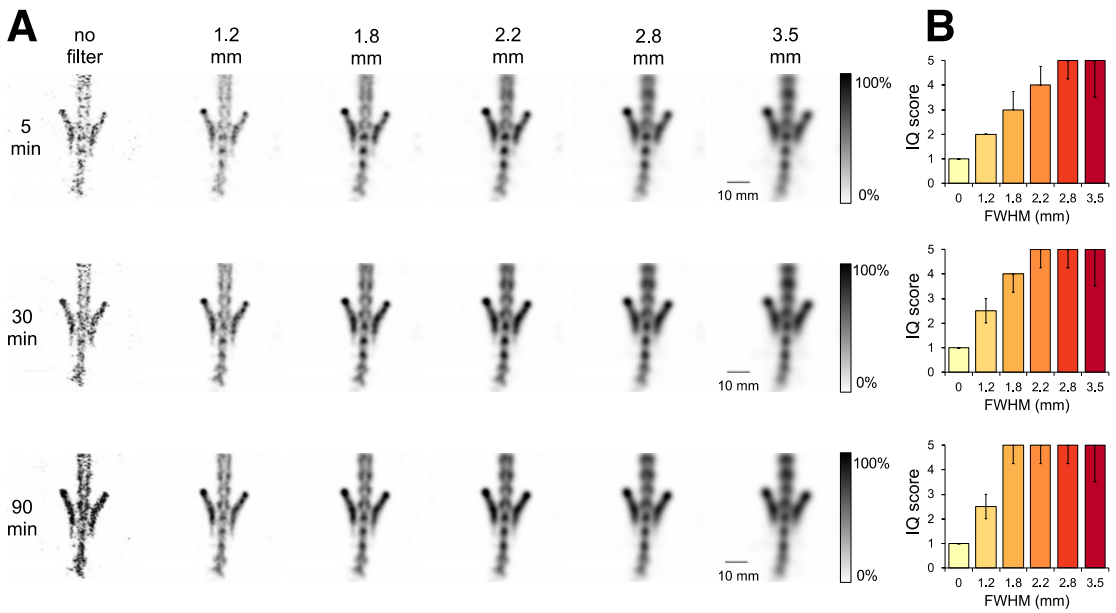


***Figure 23*** *Bone SPECT image quality assessment*

*(**A**) Overview of all bone scintigraphy images submitted to the three professional readers for evaluation. (**B**) Results of the image quality assessment. Bar charts show the image quality score (IQ score) as a function of filter size for the three different scan lengths. IQ scores are shown as median values with their respective interquartile ranges. Adapted from "Capabilities of multi-pinhole SPECT with two stationary detectors for in vivo rat imaging," by Janssen JP et al. [27].*

# 5 Discussion

In this thesis, the capabilities of rat imaging with the new small-animal U-SPECT$^5$/CT E-Class were investigated to demonstrate the potential applications of this modality and to address where this system ranks in the field of molecular imaging. It features two stationary detectors combined with multi-pinhole collimation. The main differences to the previous generations are the reduction of the detection surface by omitting the lower third detector and the new iterative reconstruction algorithm [21]. The difference to competing systems from other manufacturers is the design with stationary instead of rotating detectors [14, 15, 42, 142, 143]. Some advantages of this configuration, such as improved precession in dynamic studies and easier maintenance, have already been described [16].

## 5.1 Performance analysis

In this study, the measured sensitivity for the UHR-RM collimator was 567 cps/MBq, the maximum resolution was 1.20 mm, and the uniformity was 55.5%. Pietro et al. [141] measured with the same configuration in the U-SPECT$^6$/CT E-Class and obtained a sensitivity of 493 cps/MBq, a resolution of 0.90 mm or 1.20 mm depending on the applied reconstruction parameters and activity concentration, and a uniformity of 75.8% and 98.4% respectively. Also, van der Have et al. [16] performed a similar measurement with a comparable collimator, but they used the 3-detector system of the predecessor U-SPECT-II. They achieved a sensitivity of 700 cps/MBq and a resolution of 0.80 mm. These results appear consistent when minor differences in experimental design are taken into account, such as the much higher activity concentration of about 600 MBq/ml versus the 300 MBq/ml used for the maximum resolution assessment in this thesis. This could also explain the slightly better resolution in the results of the other two studies.

Comparing the 2-detector system with the 3-detector system, the difference seems smaller than expected, especially in terms of sensitivity. This might be due to the fact that the previous generation (U-SPECT-II, MILabs B.V., Utrecht, The Netherlands) was equipped with smaller detectors (3 x 508 mm x 381 mm x 9.5 mm vs. 2 x 472 mm x 595 mm x 9.5 mm) [16]. Thus, there is no 33% reduction in total detector area compared to this system, but only 3.3%. Therefore, a direct comparison based on the results cannot be made, nor a statement about the consequences of the missing third detector for rat imaging.

However, a direct comparison of the U-SPECT$^5$/CT E-Class with its two large detectors and the U-SPECT$^+$/CT, which has three of these detectors of the same size, has already been performed by Hoffmann et al. [145] using a general-purpose mouse collimator. The result was lower sensitivity and uniformity but with the same maximum resolution and no loss of image quality, measured as CNR. This result might also apply to rat collimators.

Other published performance evaluations using dedicated rat collimators have been carried out for the Inveon® SPECT (Siemens Healthineers AG, Erlangen, Germany) [142], the NanoSPECT® (Mediso, Budapest, Hungary) [143], the X-SPECT (Northridge Tri-Modality Imaging, Inc., Chatsworth, USA) [42] and the eXplore speCZT (GE Healthcare, Milwaukee, USA) [19, 20].

Boisson et al. [142] studied the Inveon® small-animal SPECT, which consists of two opposite detectors rotating around the target volume with 2 x 68 x 68 NaI(Tl) crystals with a size of 2 mm x 2 mm x 10 mm. They used three rat collimators: one with a single pinhole aperture (1 x 1.50 mm), and two with multi-pinhole apertures (3 x 1.20 mm vs. 3 x 1.80 mm) with three different rotation radii (50, 55, and 60 mm). Resolutions in the range of 1.20 mm to 2.00 mm and sensitivities from 53 to 175 cps/MBq were obtained.

Schramm et al. [143] investigated the NanoSPECT®, which consists of four detectors, each with 230 x 215 mm NaI(Tl) crystals rotating around the target volume. Three multi-pinhole rat collimators were examined with pinhole sizes of 1.50, 2.00, and 2.50 mm. This resulted in resolutions from 1.10 to 1.90 mm and peak sensitivities from 998 to 2229 cps/MBq. However, this study lacks background information on the applied methodology. In a more recent study, Lukas et al. [107] investigated a new generation of the NanoSPECT® but mainly described results with mouse collimators. One explanation for the system's high sensitivity is multiplexing, i.e., the use of overlapping projections. As described in the introduction, this might have negative impact on the image quality, so that a comparison based only on performance parameters is not feasible [100, 102].

Deleye et al. [42] evaluated the X-SPECT, which is part of the Triumph SPECT/PET/CT system and consists of four detectors, each with 5 x 5 CZT crystals. This results in a detection area of 4 x 127 mm x 127 mm. The rat collimator counted 20 pinholes with a respective diameter of 1.00 mm. A sensitivity of 620 cps/MBq, a spatial resolution of 0.90 mm, and a uniformity of 56% were achieved. These results are very close to those described for U-SPECT systems with stationary detectors, even though the underlying detectors differ significantly.

Mizutani et al. [20] also investigated a dedicated small-animal SPECT with ten CZT-detectors, each with a 78.7 x 78.7 $mm^2$ detection surface. These were stationary and arranged circularly around a rotating collimator. The used rat collimators had five pinholes with 1.00- and 1.50-millimeter diameters. A sensitivity of 138 cps/MBq and 321 cps/MBq, respectively, as well as a maximum resolution of 1.20 and 1.50 mm were determined.

One limitation to performance evaluation is that a standard for micro-SPECT has yet to be established. Therefore, only the guidelines for clinical gamma cameras and small animal PET could be taken as reference [56, 126]. This problem has been discussed several times in the literature [127, 128] and is a reasonable explanation for the different results of the other performance assessments. For example, Prieto et al. [141] calculated a substantially different value for uniformity under nearly identical conditions (>75% vs. 55.5%). This is most likely due to variations in the voxel size and post-processing. While Prieto et al. calculated the uniformity based on unfiltered images, in this thesis a post-filter with an FWHM of the maximum resolution was applied before uniformity calculation. Another issue that makes comparability difficult is that in some studies, the maximum resolution is determined by visual assessment of hot-rod phantoms. In contrast, in other studies, the FWHM of a line source is being measured [146].

In summary, the performance evaluation results are comparable with slight improvements to other established systems. There is not a significant disadvantage due to the missing third detector. Also, a maximum resolution of up to 0.80 mm could be achieved with a very high activity concentration of >500 MBq/ml. Still, it must be emphasized that such high activity concentrations are not realistic for in vivo experiments. A compilation of all these performance parameters of the different SPECT systems for rat imaging is listed in ***Table 2***.

## 5.2 In vitro image quality

For in vitro image quality analysis, the CNR value was calculated based on the method introduced by Walker et al. [90]. The obtained values increased with growing rod size and activity concentration. For the area below the maximum resolution CNR was very small or even negative. Walker et al. also reported the same finding for pinhole PET.

When interpreting CNR values, the following considerations can be made to assess how the values apply to imaging in practice. To perceive a region as well-resolved, at least a value equal to the CNR achieved for peak resolution (>1.5) should be obtained. If the

image noise is too high due to poor counting statistics and hence the CNR is simply not sufficient, the post-filter must be increased. In this case, the post-filter limits the maximum resolution by its size (FWHM = maximum resolution). This yields in a realistic resolution range for low activity concentrations with sufficiently large CNR. Thus, for 1.0 MBq/ml, 0.5 MBq/ml, and 0.1 MBq/ml as activity concentration, rods with ≥1.80 mm, ≥2.00 mm, and with ≥2.80 mm, respectively, were sufficiently resolved.

Hoffmann et al. [145] and Matsusaka et al. [147] used the identical technique for the U-SPECT$^5$/CT E-Class, although they focused on dedicated collimators for mice and medium-sized animals, respectively. In their studies, the same correlations were found. Moreover, the CNR values of the smallest resolved rod sizes were about 1.5 for the respective collimators investigated. It was demonstrated that the high-resolution mouse collimators require a substantial number of counts to meet their specifications due to their low sensitivity. Consequently, these are particularly suitable for high injection doses, long measurement times, and focused scans. These results could also apply to rat imaging, so a general-purpose or high-sensitivity rat collimator may be more suitable for some applications than the UHR-RM collimator investigated in this thesis.

In addition to the parameters assessed, the U-SPECT$^6$/CT E-Class, which is nearly identical to the U-SPECT$^5$/CT E-Class, has demonstrated that the system can accurately quantify activity in the target volume and that multiple isotopes can be imaged simultaneously with sufficient quality and quantification [141]. Their paper also showed a better result for imaging multiple radioisotopes than the NanoSPECT® investigated by Lukas et al. [107].

## 5.3 In vivo image quality

Analysis of myocardial perfusion SPECT images showed that CNR increased substantially between 10 and 30 min, but further extension of scan duration to 60 min resulted in a slight increase compared to the 30-minute scan. The outcome of the image quality assessment by professional readers were similar. Again, increasing the scan duration did not significantly improve the IQ scores assigned, and the 60-minute scans were rated worse. The slightly more intense scaling could explain this poorer image impression.

Compared to the acquisition time, the effect of the post-filter on the image quality was far more prominent. For all scans, very good results were obtained with 3.5 and 4.0 mm

FWHM Gaussian filters, and the values in this range were accordingly highest for CNR as well as subjective IQ scores. If a higher resolution is required in certain studies, the Gaussian filter can be easily reduced to about 2.2 mm FWHM, because even then a perfectly adequate image quality can be achieved.

Mizutani et al. [20] also investigated the relationship between injection dose and filter size on image quality in myocardial perfusion SPECT. However, as described above, this was investigated using a system with CZT detectors and two collimators consisting of five pinholes each. In this study, the evaluation by two professional readers showed an improvement in image quality by increasing the injection doses from 25 MBq to 200 MBq and by adjusting the Gaussian filter from unfiltered to FWHM of 1.5 mm to FWHM of 2.5 mm. In this case, the impact of the injection doses was greater compared to the filter. However, it must be considered that there are other influencing factors, such as the reconstruction algorithm and the voxel size. Overall, the results are in line with ours.

In bone SPECT, increasing the post-filter sizes resulted in better CNR, although the anatomical structures appeared blurred. This could indicate that using ROIs to assess in vivo image quality may be limited. Especially for finer bone structures, the tracer distribution could suggest a false high noise level. Nevertheless, the subjective IQ score also showed a significant improvement in image quality by increasing the post-filter, especially in the range between 1.2 mm and 1.8 mm FWHM. At the same time, there were few differences between 5, 30, and 90 min of scan time.

The in vivo studies demonstrated that the system could acquire high-quality myocardial perfusion and bone SPECT images in rats. The strong effect of the size of the Gaussian filter on CNR and image quality in all images might be explained mainly by the reduction of noise and the improvement of uniformity [18]. Translating the in vitro image quality analysis to animal studies is challenging. Still, the count statistics in the uptaking target structures of the longest in vivo measurements (60 and 90 min) are comparable to the phantom measurement at 1.0 MBq/ml. This phantom measurement could resolve structures up to 1.80 mm in good quality. In the animal studies, a good increase in CNR values, as well as an assessment of image quality by the professional readers with “moderate” to “good” was achieved from a filter range of FWHM ≥1.8 mm (bone) or FWHM ≥2.2 mm (myocardium).

Thus, a realistic resolution with good image quality of ≥1.80 mm can be assumed for studies similar to our protocol; to achieve the maximum resolution of 1.20 mm, significantly higher injection doses, longer acquisition times, or focused scans with less bed positions would be essential.

The results of the in vivo experiments are limited to using only one rat for each tracer. Since the focus of this thesis was on image quality and the influence of scan time and post-filter, it was decided to analyze only two examples with clinically relevant and well-established tracers and sufficient tracer uptake. Further, this also avoids using an unnecessarily large number of experimental animals. Results are expected to vary between different laboratory animals, which should also be of particular interest when investigating quantitative accuracy. Another limitation is that only a specific count range was covered with one whole-body heart scan and one focused bone scan. Although the range was extensive, achieving superior results with highly focused scans, longer scan times, and higher injection doses may still be possible. However, this might be more appropriate for ex vivo protocols. On the other hand, lower injection doses, shorter scan times, or dynamic scans could lead to inferior results. In this case, using a collimator with higher sensitivity is recommended at the expense of maximum resolution.

## 5.4 SPECT vs. PET for molecular imaging in rodents

In the following, the advantages and disadvantages of PET and SPECT technology from Section 1.5 are briefly reviewed with respect to the investigated system and the field of molecular imaging in rats.

As demonstrated, the U-SPECT$^5$/CT E-Class is capable of high-quality imaging of myocardial perfusion and bone metabolism in rats. The UHR-RM collimator enabled a resolution of up to 1.80 mm with good image quality.

This result relativizes the superiority of SPECT over PET in terms of the maximum resolution in small-animal imaging. While resolutions of 0.80 mm for rat collimators [16] and 0.25 mm for mouse collimators [11] have been described in phantom studies, these are not realistically achievable in rats due to limited sensitivity.

Consequently, PET and SPECT are both suitable for many applications in rats, as $^{18}$F-based tracers allow resolutions in a similar range of 1.61 to 2.34 mm but with one to two orders of magnitude higher sensitivity than SPECT [148]. Thus, if good PET-based alternatives are available, like $^{18}$F-FDG for myocardial perfusion and $^{18}$F-NaF for bone metabolism, these might provide comparable results with lower injection doses and shorter acquisition times [72, 78, 79]. Similar conclusions were also made by Meester et

al. [149] in their review on radionuclide imaging of atherosclerosis in small animals. However, in mice or ex vivo studies, the advantage of high-resolution SPECT is likely more apparent due to the smaller FOV and associated higher magnification or the possibility of very long scan times.

For this purpose, the recent introduction of pinhole PET, which is reported to allow resolutions of up to 0.85 mm with a sensitivity of 3700 cps/MBq could be promising even though it reduces the excellent sensitivity of PET technology [90]. Further investigation is required regarding the extent to which study protocols might benefit from this technology.

It must be emphasized that the key advantages of SPECT technology remain: simultaneous imaging of multiple radioisotopes [9, 107, 141] and an extensive range of well-researched and easily accessible radiotracers [49].

## 5.5 Conclusion

In this thesis, the performance of the U-SPECT$^5$/CT E-Class with two stationary detectors and one multi-pinhole collimator for rat imaging was evaluated. The system provides a maximum resolution of 1.20 mm with a sensitivity of 567 cps/MBq and a uniformity of 55.5%, placing its performance on par if not better than the systems described in the literature. Phantom image quality assessment revealed that resolution at activity concentrations corresponding to in vivo protocols is more in the range of 1.80 to 2.80 mm to achieve good image quality. It was shown that a suitable post-filter has a decisive influence on image quality. This result was confirmed in respective in vivo images by CNR calculation and evaluation of professional readers.

The SPECT system is suitable for molecular imaging in rats and achieved excellent cardiac and bone scan results. While a more sensitive collimator or PET might be a good choice for low-activity studies, the U-SPECT$^5$/CT E-Class with the UHR-RM collimator is currently among the best options for radionuclide imaging in rats for high-activity or focused scans.

## 5.6 Outlook

In addition to the properties of the U-SPECT$^5$/CT E-Class investigated in this thesis, some open questions would be interesting to answer. One of them is the quantitative accuracy of the system, which has already been studied in mice and showed very accurate results [141]. Also, the possibilities for dynamic studies, as already performed

with the same system using a medium-sized animal collimator in rats and rabbits [147], could be further investigated.

Special attention should also be paid to the capabilities of multi-isotope imaging, as this is a crucial advantage of SPECT; work in this area has so far been mainly performed with mice [107, 141].

Prieto et al. [141] have studied how well multiple mice can be scanned simultaneously in a rat collimator; this approach could also be interesting for studying multiple rats simultaneously in a larger collimator, especially if an excessively high resolution is not required.

Further development of existing technologies and innovations will continue to improve the performance and capabilities of molecular imaging in rats. Larger detectors with magnification factors like those achieved in mice, and especially improvements in detector technology, could further improve the resolution range and sensitivity. In particular, the use of big CZT crystals, as already used in some clinical settings, remains promising [9, 111]. Further development of iterative reconstruction algorithms, such as the recently introduced dual-voxel dual-matrix approach, which further accelerates reconstruction and enables processing of even larger data sets, also shows how rapidly the research field is evolving [150].

However, to ensure the quality and comparability of different small-animal SPECT systems, a standard must be created as soon as possible, as already exists for small-animal PET and clinical devices [56, 126-128].

# 6 Summary

Molecular imaging of rats is of great importance for basic and translational research. As a powerful tool in nuclear medicine, SPECT can be used to visualize specific functional processes in the body, such as myocardial perfusion or bone metabolism. Typical applications in laboratory animals are imaging diagnostics or the development of new tracers for clinical use. Innovations have enabled resolutions of up to a quarter of a millimeter with acceptable sensitivity. These advances have recently led to significantly more interest in SPECT both clinically and preclinically.

The objective of this thesis was to evaluate the performance of the new U-SPECT$^5$/CT E-Class by MILabs with a dedicated ultra-high resolution multi-pinhole collimator for rats and its potential for in vivo imaging of rats. The unique features of the U-SPECT are the large stationary detectors and the new iterative reconstruction algorithm. In addition, compared to the conventional system, the "E-Class" uses only two detectors instead of three.

First, the sensitivity, maximum resolution, and uniformity were determined as performance parameters. Thereafter, CNRs for different activity levels comparable to those of typical in vivo activities were examined. Finally, two example protocols were carried out for imaging with $^{99m}$Tc-MIBI and $^{99m}$Tc-HMDP in healthy rats to evaluate the in vivo capabilities. For this purpose, CNR calculations and an image quality assessment were performed. The focus was on image quality as a function of scan time and post-reconstruction filter across a wide range of realistically achievable in vivo conditions.

Performance was reasonable compared to other systems in the literature, with a sensitivity of 567 cps/MBq, a maximum resolution of 1.20 mm, and a uniformity of 55.5%. At the lower activities, resolution in phantom studies decreased to ≥1.80 mm while maintaining good image quality. High-quality bone and myocardial perfusion SPECTs were obtained in rats with a resolution of ≥1.80 mm and ≥2.20 mm, respectively. Although limited sensitivity remains a weakness of SPECT, the U-SPECT$^5$/CT E-Class with the UHR-RM collimator can achieve in vivo results of the highest standard despite the missing third detector. Currently, it is one of the best options for high-resolution radionuclide imaging in rats.

# Zusammenfassung

Die molekulare Bildgebung bei Ratten hat einen hohen Stellenwert in der Grundlagenforschung und der translationale Forschung. Dabei ist SPECT ein leistungsfähiges Instrument zur Visualisierung spezifischer funktioneller Prozesse im Körper, wie z. B. der Herzmuskeldurchblutung oder des Knochenstoffwechsels. Typische Anwendungsbereiche an Labortieren sind die bildgebende Diagnostik im Rahmen von Studien oder die Entwicklung neuer Tracer für den klinischen Einsatz. Durch Innovationen wurden Auflösungen von bis zu einem Viertelmillimeter bei akzeptabler Empfindlichkeit erreichbar. Diese Fortschritte haben in letzter Zeit zu einem deutlich gestiegenen Interesse an SPECT sowohl im klinischen als auch im präklinischen Bereich geführt.

Ziel dieser Arbeit war es, die Leistung des neuen U-SPECT$^5$/CT E-Class von MILabs mit einem speziellen ultra-hochauflösenden Multi-Pinhole-Kollimator für Ratten und das Potenzial für die In-vivo-Bildgebung bei Ratten zu untersuchen. Dabei sind die Besonderheiten des U-SPECTs die großen stationären Detektoren und der neue iterative Rekonstruktionsalgorithmus. Außerdem verfügt die von uns verwendete „E-Klasse“ im Vergleich zum konventionellen System nur über zwei statt drei Detektoren.

Zunächst wurden die Sensitivität, die maximale Ortsauflösung und die Homogenität als Leistungsparameter bestimmt. Anschließend wurde das Kontrast-Rausch-Verhältnis für verschiedene Aktivitätsniveaus, die mit denen typischer In-vivo-Studien vergleichbar sind, untersucht. Schließlich wurden zwei Beispielprotokolle für die Bildgebung mit $^{99m}$Tc-MIBI und $^{99m}$Tc-HMDP bei gesunden Ratten durchgeführt, um die In-vivo-Kapazitäten zu erfassen. Zur Bewertung wurden eine Kontrast-Rausch-Analyse und eine Bildqualitätsumfrage genutzt. Der Schwerpunkt lag dabei auf der Bildqualität in Abhängigkeit von der Scanzeit sowie dem Postrekonstruktionsfilters für ein breites Spektrum realistisch erreichbarer In-vivo-Bedingungen.

Die Leistung war mit einer Sensitivität von 567 cps/MBq, einer maximalen Ortsauflösung von 1,20 mm und einer Homogenität von 55,5% mit anderen in der Literatur beschriebenen Systemen vergleichbar. Bei niedrigeren Aktivitäten verringerte sich die Auflösung in Phantomstudien auf ≥1,80 mm bei gleichbleibend guter Bildqualität. Es wurden hochqualitative Knochen- und Myokardperfusions-SPECTs mit einer Auflösung

von ≥1,80 mm bzw. ≥2,20 mm bei Ratten erzielt. Obwohl die begrenzte Empfindlichkeit nach wie vor eine Schwäche der SPECT ist, kann das U-SPECT$^5$/CT E-Class mit dem UHR-RM-Kollimator, trotz des fehlenden dritten Detektors, In-vivo-Ergebnisse auf höchstem Niveau erzielen. Es ist derzeit eine der besten Optionen für die hochauflösende Radionuklid-Bildgebung bei Ratten.

# 7 References


[1] T. F. Massoud and S. S. Gambhir, "Molecular imaging in living subjects: seeing fundamental biological processes in a new light," *Genes Dev,* vol. 17, no. 5, pp. 545-80, Mar 1 2003, doi: 10.1101/gad.1047403.

[2] M. A. Pysz, S. S. Gambhir, and J. K. Willmann, "Molecular imaging: current status and emerging strategies," (in eng), *Clin Radiol,* vol. 65, no. 7, pp. 500-16, Jul 2010, doi: 10.1016/j.crad.2010.03.011.

[3] S. R. Meikle, P. Kench, M. Kassiou, and R. B. Banati, "Small animal SPECT and its place in the matrix of molecular imaging technologies," *Phys Med Biol,* vol. 50, no. 22, pp. R45-61, Nov 21 2005, doi: 10.1088/0031-9155/50/22/R01.

[4] B. L. Franc, P. D. Acton, C. Mari, and B. H. Hasegawa, "Small-animal SPECT and SPECT/CT: important tools for preclinical investigation," *Journal of nuclear medicine : official publication, Society of Nuclear Medicine,* vol. 49, no. 10, pp. 1651-63, Oct 2008, doi: 10.2967/jnumed.108.055442.

[5] G. D. Hutchins, M. A. Miller, V. C. Soon, and T. Receveur, "Small animal PET imaging," (in eng), *Ilar j,* vol. 49, no. 1, pp. 54-65, 2008, doi: 10.1093/ilar.49.1.54.

[6] N. J. Serkova *et al.*, "Preclinical Applications of Multi-Platform Imaging in Animal Models of Cancer," *Cancer Research,* vol. 81, no. 5, pp. 1189-1200, 2021, doi: 10.1158/0008-5472.Can-20-0373.

[7] M. D. Farwell, D. A. Pryma, and D. A. Mankoff, "PET/CT imaging in cancer: current applications and future directions," *Cancer,* vol. 120, no. 22, pp. 3433-45, Nov 15 2014, doi: 10.1002/cncr.28860.

[8] F. Nensa, K. Beiderwellen, P. Heusch, and A. Wetter, "Clinical applications of PET/MRI: current status and future perspectives," *Diagn Interv Radiol,* vol. 20, no. 5, pp. 438-47, Sep-Oct 2014, doi: 10.5152/dir.2014.14008.

[9] T. Van den Wyngaert, F. Elvas, S. De Schepper, J. A. Kennedy, and O. Israel, "SPECT/CT: Standing on the Shoulders of Giants, It Is Time to Reach for the Sky!," *Journal of Nuclear Medicine,* vol. 61, no. 9, pp. 1284-1291, 2020, doi: 10.2967/jnumed.119.236943.

[10] O. Ivashchenko, F. van der Have, M. C. Goorden, R. M. Ramakers, and F. J. Beekman, "Ultra-high-sensitivity submillimeter mouse SPECT," (in eng), *Journal of nuclear medicine : official publication, Society of Nuclear Medicine,* vol. 56, no. 3, pp. 470-5, Mar 2015, doi: 10.2967/jnumed.114.147140.

[11] O. Ivashchenko *et al.*, "Quarter-millimeter-resolution molecular mouse imaging with U-SPECT(+)," *Mol Imaging,* vol. 13, 2014, doi: 10.2310/7290.2014.00053.

[12] M. A. King, P. H. Pretorius, T. Farncombe, and F. J. Beekman, "Introduction to the physics of molecular imaging with radioactive tracers in small animals," *J Cell Biochem Suppl,* vol. 39, pp. 221-30, 2002, doi: 10.1002/jcb.10447.

[13] F. Beekman and F. van der Have, "The pinhole: gateway to ultra-high-resolution three-dimensional radionuclide imaging," *European journal of nuclear medicine and molecular imaging,* vol. 34, no. 2, pp. 151-61, Feb 2007, doi: 10.1007/s00259-006-0248-6.

[14] L. R. Furenlid *et al.*, "FastSPECT II: A Second-Generation High-Resolution Dynamic SPECT Imager," *IEEE Trans Nucl Sci,* vol. 51, no. 3, pp. 631-635, Jun 2004, doi: 10.1109/TNS.2004.830975.

[15] B. Vastenhouw and F. Beekman, "Submillimeter total-body murine imaging with U-SPECT-I," *Journal of nuclear medicine : official publication, Society of Nuclear Medicine,* vol. 48, no. 3, pp. 487-93, Mar 2007. [Online]. Available: https://www.ncbi.nlm.nih.gov/pubmed/17332628 http://jnm.snmjournals.org/content/48/3/487.full.pdf.

[16] F. van der Have *et al.*, "U-SPECT-II: An Ultra-High-Resolution Device for Molecular Small-Animal Imaging," *Journal of nuclear medicine : official publication, Society of Nuclear Medicine,* vol. 50, no. 4, pp. 599-605, Apr 2009, doi: 10.2967/jnumed.108.056606.

[17] Y. Higaki, M. Kobayashi, T. Uehara, H. Hanaoka, Y. Arano, and K. Kawai, "Appropriate collimators in a small animal SPECT scanner with CZT detector," *Ann Nucl Med,* vol. 27, no. 3, pp. 271-8, Apr 2013, doi: 10.1007/s12149-012-0681-5.

[18] A. A. Harteveld *et al.*, "Using the NEMA NU 4 PET image quality phantom in multipinhole small-animal SPECT," *Journal of nuclear medicine : official publication, Society of Nuclear Medicine,* vol. 52, no. 10, pp. 1646-53, Oct 2011, doi: 10.2967/jnumed.110.087114.

[19] I. Matsunari *et al.*, "Performance evaluation of the eXplore speCZT preclinical imaging system," *Ann Nucl Med,* vol. 28, no. 5, pp. 484-97, Jun 2014, doi: 10.1007/s12149-014-0828-7.

[20] A. Mizutani *et al.*, "Impact of injection dose, post-reconstruction filtering, and collimator choice on image quality of myocardial perfusion SPECT using cadmium-zinc telluride detectors in the rat," *EJNMMI Phys,* vol. 2, no. 1, p. 7, Dec 2015, doi: 10.1186/s40658-015-0111-6.

[21] P. E. Vaissier, F. J. Beekman, and M. C. Goorden, "Similarity-regulation of OS-EM for accelerated SPECT reconstruction," *Phys Med Biol,* vol. 61, no. 11, pp. 4300-15, Jun 7 2016, doi: 10.1088/0031-9155/61/11/4300.

[22] P. M. Iannaccone and H. J. Jacob, "Rats!," *Dis Model Mech,* vol. 2, no. 5-6, pp. 206-10, May-Jun 2009, doi: 10.1242/dmm.002733.

[23] J. R. Homberg, M. Wöhr, and N. Alenina, "Comeback of the Rat in Biomedical Research," *ACS Chemical Neuroscience,* vol. 8, no. 5, pp. 900-903, 2017/05/17 2017, doi: 10.1021/acschemneuro.6b00415.

[24] A. G. Jones *et al.*, "Biological studies of a new class of technetium complexes: the hexakis(alkylisonitrile)technetium(I) cations," *Int J Nucl Med Biol,* vol. 11, no. 3-4, pp. 225-34, 1984, doi: 10.1016/0047-0740(84)90004-4.

[25] J. A. Bevan, A. J. Tofe, J. J. Benedict, M. D. Francis, and B. L. Barnett, "Tc-99m HMDP (hydroxymethylene diphosphonate): a radiopharmaceutical for skeletal and acute myocardial infarct imaging. I. Synthesis and distribution in animals," *Journal of nuclear medicine : official publication, Society of Nuclear Medicine,* vol. 21, no. 10, pp. 961-6, Oct 1980. [Online]. Available: https://www.ncbi.nlm.nih.gov/pubmed/6252298.

[26] J. A. Bevan, A. J. Tofe, J. J. Benedict, M. D. Francis, and B. L. Barnett, "Tc-99m HMDP (hydroxymethylene diphosphonate): a radiopharmaceutical for skeletal and acute myocardial infarct imaging. II. Comparison of Tc-99m hydroxymethylene diphosphonate (HMDP) with other technetium-labeled bone-imaging agents in a canine model," *Journal of nuclear medicine : official publication, Society of Nuclear Medicine,* vol. 21, no. 10, pp. 967-70, Oct 1980. [Online]. Available: https://www.ncbi.nlm.nih.gov/pubmed/6252299.

[27] J. P. Janssen *et al.*, "Capabilities of multi-pinhole SPECT with two stationary detectors for in vivo rat imaging," *Sci Rep,* vol. 10, no. 1, p. 18616, Oct 29 2020, doi: 10.1038/s41598-020-75696-0.

[28] D. A. Mankoff, "A definition of molecular imaging," *Journal of nuclear medicine : official publication, Society of Nuclear Medicine,* vol. 48, no. 6, pp. 18N, 21N, Jun 2007. [Online]. Available: https://www.ncbi.nlm.nih.gov/pubmed/17536102.

[29] M. Sonia Marta, K. Kátia Hiromoto, T. Paulo Henrique Alves, and S. Marcelo José dos, "Clinical Applications of Nuclear Medicine," in *Medical Imaging in Clinical Practice*, E. Okechukwu Felix Ed. Rijeka: IntechOpen, 2013, p. Ch. 3.

[30] N. Oriuchi, H. Endoh, and K. Kaira, "Monitoring of Current Cancer Therapy by Positron Emission Tomography and Possible Role of Radiomics Assessment," *Int J Mol Sci,* vol. 23, no. 16, Aug 20 2022, doi: 10.3390/ijms23169394.
[31] A. K. Buck *et al.*, "SPECT/CT," *Journal of Nuclear Medicine,* vol. 49, no. 8, pp. 1305-1319, 2008, doi: 10.2967/jnumed.107.050195.
[32] G. Mariani *et al.*, "A review on the clinical uses of SPECT/CT," *European journal of nuclear medicine and molecular imaging,* vol. 37, no. 10, pp. 1959-85, Oct 2010, doi: 10.1007/s00259-010-1390-8.
[33] I. M. Desar, C. M. van Herpen, H. W. van Laarhoven, J. O. Barentsz, W. J. Oyen, and W. T. van der Graaf, "Beyond RECIST: molecular and functional imaging techniques for evaluation of response to targeted therapy," *Cancer Treat Rev,* vol. 35, no. 4, pp. 309-21, Jun 2009, doi: 10.1016/j.ctrv.2008.12.001.
[34] T. A. Dragani *et al.*, "Major milestones in translational oncology," *BMC Med,* vol. 14, no. 1, p. 110, Jul 28 2016, doi: 10.1186/s12916-016-0654-y.
[35] A. Wirrwar, N. Schramm, H. Vosberg, and H. W. Müller-Gärtner, "High resolution SPECT in small animal research," (in eng), *Rev Neurosci,* vol. 12, no. 2, pp. 187-93, 2001, doi: 10.1515/revneuro.2001.12.2.187.
[36] N. Galldiks *et al.*, "Treatment monitoring of immunotherapy and targeted therapy using FET PET in patients with melanoma and lung cancer brain metastases: Initial experiences," *Journal of Clinical Oncology,* vol. 37, no. 15_suppl, pp. e13525-e13525, 2019, doi: 10.1200/JCO.2019.37.15_suppl.e13525.
[37] T. E. Peterson and L. R. Furenlid, "SPECT detectors: the Anger Camera and beyond," *Phys Med Biol,* vol. 56, no. 17, pp. R145-82, Sep 7 2011, doi: 10.1088/0031-9155/56/17/R01.
[38] T. Aitman, P. Dhillon, and A. M. Geurts, "A RATional choice for translational research?," *Dis Model Mech,* vol. 9, no. 10, pp. 1069-1072, Oct 1 2016, doi: 10.1242/dmm.027706.
[39] B. Ellenbroek and J. Youn, "Rodent models in neuroscience research: is it a rat race?," *Dis Model Mech,* vol. 9, no. 10, pp. 1079-1087, Oct 1 2016, doi: 10.1242/dmm.026120.
[40] C. P. Muller and J. R. Homberg, "The role of serotonin in drug use and addiction," *Behav Brain Res,* vol. 277, pp. 146-92, Jan 15 2015, doi: 10.1016/j.bbr.2014.04.007.
[41] N. Hayakawa *et al.*, "Impact of tissue photon attenuation in small animal cardiac PET imaging," *Int J Cardiol,* vol. 227, pp. 257-260, Jan 15 2017, doi: 10.1016/j.ijcard.2016.11.119.
[42] S. Deleye, R. Van Holen, J. Verhaeghe, S. Vandenberghe, S. Stroobants, and S. Staelens, "Performance evaluation of small-animal multipinhole muSPECT scanners for mouse imaging," *European journal of nuclear medicine and molecular imaging,* vol. 40, no. 5, pp. 744-58, May 2013, doi: 10.1007/s00259-012-2326-2.
[43] D. L. Bailey, J. L. Humm, A. Todd-Porkopek, and A. van Aswegen, *Nuclear Medicine Physics: A Handbook for Teachers and Students*. Vienna: International Atomic Energy Agency, 2014.
[44] S. Liu, "Bifunctional coupling agents for radiolabeling of biomolecules and target-specific delivery of metallic radionuclides," *Adv Drug Deliv Rev,* vol. 60, no. 12, pp. 1347-70, Sep 2008, doi: 10.1016/j.addr.2008.04.006.
[45] D. Papagiannopoulou, "Technetium-99m radiochemistry for pharmaceutical applications," *J Labelled Comp Radiopharm,* vol. 60, no. 11, pp. 502-520, Sep 2017, doi: 10.1002/jlcr.3531.

[46] U. National Research Council Committee on Medical Isotope Production Without Highly Enriched, in *Medical Isotope Production without Highly Enriched Uranium*. Washington (DC): National Academies Press (US)
Copyright 2009 by the National Academy of Sciences. All rights reserved., 2009.
[47] W. D. Tucker, M. W. Greene, A. J. Weiss, and A. Murrenhoff, "Methods of preparation of some carrier-free radioisotopes involving sorption on alumina," United States, 1958. [Online]. Available: https://www.osti.gov/biblio/4305138 https://www.osti.gov/servlets/purl/4305138
[48] V. Drozdovitch *et al.*, "Use of radiopharmaceuticals in diagnostic nuclear medicine in the United States: 1960-2010," *Health Phys,* vol. 108, no. 5, pp. 520-37, May 2015, doi: 10.1097/HP.0000000000000261.
[49] A. Duatti, "Review on (99m)Tc radiopharmaceuticals with emphasis on new advancements," *Nucl Med Biol,* vol. 92, pp. 202-216, Jan 2021, doi: 10.1016/j.nucmedbio.2020.05.005.
[50] C. Bolzati and A. Dolmella, "Nitrido Technetium-99 m Core in Radiopharmaceutical Applications: Four Decades of Research," *Inorganics,* vol. 8, no. 1, p. 3, 2020. [Online]. Available: https://www.mdpi.com/2304-6740/8/1/3.
[51] S. M. Rathmann, Z. Ahmad, S. Slikboer, H. A. Bilton, D. P. Snider, and J. F. Valliant, "The Radiopharmaceutical Chemistry of Technetium-99m," in *Radiopharmaceutical Chemistry*, J. S. Lewis, A. D. Windhorst, and B. M. Zeglis Eds. Cham: Springer International Publishing, 2019, pp. 311-333.
[52] O. Israel *et al.*, "Two decades of SPECT/CT - the coming of age of a technology: An updated review of literature evidence," *European journal of nuclear medicine and molecular imaging,* vol. 46, no. 10, pp. 1990-2012, Sep 2019, doi: 10.1007/s00259-019-04404-6.
[53] "The Supply of Medical Radioisotopes: Medical Isotope Demand and Capacity Projection for the 2018–2023 Period," presented at the OECD Nuclear Energy Agency, Paris, France, 2018.
[54] "Diagnostic nuclear medicine." Bundesamt für Strahlenschutz. https://www.bfs.de/DE/themen/ion/anwendung-medizin/diagnostik/nuklearmedizin/nuklearmedizin_node.html (accessed 23.10.2022, 2022).
[55] L. Giovanella *et al.*, "EANM practice guideline/SNMMI procedure standard for RAIU and thyroid scintigraphy," *European journal of nuclear medicine and molecular imaging,* vol. 46, no. 12, pp. 2514-2525, Nov 2019, doi: 10.1007/s00259-019-04472-8.
[56] *National Eletrical Manufacturers Association in NEMA Standards Publication NU 1-2018: Performance Measurements of Gamma Cameras*. Rosslyn (VA), 2019.
[57] A. K. Paul and H. A. Nabi, "Gated myocardial perfusion SPECT: basic principles, technical aspects, and clinical applications," (in eng), *J Nucl Med Technol,* vol. 32, no. 4, pp. 179-87; quiz 188-9, Dec 2004.
[58] J. D. Kelly *et al.*, "Technetium-99m-Tetrofosmin as a New Radiopharmaceutical for Myocardial Perfusion Imaging," *Journal of Nuclear Medicine,* vol. 34, no. 2, pp. 222-227, 1993. [Online]. Available: https://jnm.snmjournals.org/content/jnumed/34/2/222.full.pdf.
[59] O. Lindner *et al.*, "[Myokard-Perfusions-SPECT. Myocardial perfusion SPECT - Update S1 guideline]," *Nuklearmedizin,* vol. 56, no. 4, pp. 115-123, Aug 14 2017, doi: 10.3413/Nukmed-2017040001. Myokard-Perfusions-SPECT. Update S1-Leitlinie(1).
[60] H. J. Verberne *et al.*, "EANM procedural guidelines for radionuclide myocardial perfusion imaging with SPECT and SPECT/CT: 2015 revision," *European journal of nuclear medicine and molecular imaging,* vol. 42, no. 12, pp. 1929-40, Nov 2015, doi: 10.1007/s00259-015-3139-x.

[61] M. D. Cerqueira *et al.*, "Standardized myocardial segmentation and nomenclature for tomographic imaging of the heart. A statement for healthcare professionals from the Cardiac Imaging Committee of the Council on Clinical Cardiology of the American Heart Association," *Circulation,* vol. 105, no. 4, pp. 539-42, Jan 29 2002, doi: 10.1161/hc0402.102975.

[62] J. Knuuti *et al.*, "2019 ESC Guidelines for the diagnosis and management of chronic coronary syndromes," *Eur Heart J,* vol. 41, no. 3, pp. 407-477, Jan 14 2020, doi: 10.1093/eurheartj/ehz425.

[63] S. S. Virani *et al.*, "Heart Disease and Stroke Statistics-2021 Update: A Report From the American Heart Association," *Circulation,* vol. 143, no. 8, pp. e254-e743, Feb 23 2021, doi: 10.1161/CIR.0000000000000950.

[64] R. C. Cury *et al.*, "CAD-RADS(TM) Coronary Artery Disease - Reporting and Data System. An expert consensus document of the Society of Cardiovascular Computed Tomography (SCCT), the American College of Radiology (ACR) and the North American Society for Cardiovascular Imaging (NASCI). Endorsed by the American College of Cardiology," *J Cardiovasc Comput Tomogr,* vol. 10, no. 4, pp. 269-81, Jul-Aug 2016, doi: 10.1016/j.jcct.2016.04.005.

[65] S. R. Underwood *et al.*, "Myocardial perfusion scintigraphy: the evidence," *European journal of nuclear medicine and molecular imaging,* vol. 31, no. 2, pp. 261-91, Feb 2004, doi: 10.1007/s00259-003-1344-5.

[66] L. J. Shaw and A. E. Iskandrian, "Prognostic value of gated myocardial perfusion SPECT," *Journal of nuclear cardiology : official publication of the American Society of Nuclear Cardiology,* vol. 11, no. 2, pp. 171-85, Mar-Apr 2004, doi: 10.1016/j.nuclcard.2003.12.004.

[67] J. M. Baron and P. Chouraqui, "Myocardial single-photon emission computed tomographic quality assurance," *Journal of nuclear cardiology : official publication of the American Society of Nuclear Cardiology,* vol. 3, no. 2, pp. 157-66, Mar-Apr 1996, doi: 10.1016/s1071-3581(96)90008-2.

[68] D. S. Berman *et al.*, "Underestimation of extent of ischemia by gated SPECT myocardial perfusion imaging in patients with left main coronary artery disease," *Journal of nuclear cardiology : official publication of the American Society of Nuclear Cardiology,* vol. 14, no. 4, pp. 521-8, Jul 2007, doi: 10.1016/j.nuclcard.2007.05.008.

[69] A. J. Einstein, K. W. Moser, R. C. Thompson, M. D. Cerqueira, and M. J. Henzlova, "Radiation dose to patients from cardiac diagnostic imaging," *Circulation,* vol. 116, no. 11, pp. 1290-305, Sep 11 2007, doi: 10.1161/CIRCULATIONAHA.107.688101.

[70] R. Taillefer, "Clinical applications of 99mTc-sestamibi scintimammography," *Seminars in nuclear medicine,* vol. 35, no. 2, pp. 100-15, Apr 2005, doi: 10.1053/j.semnuclmed.2004.11.002.

[71] C. H. Han, C. H. Fry, P. Sharma, and T. S. Han, "A clinical perspective of parathyroid hormone related hypercalcaemia," *Rev Endocr Metab Disord,* vol. 21, no. 1, pp. 77-88, Mar 2020, doi: 10.1007/s11154-019-09529-5.

[72] M. W. Parker *et al.*, "Diagnostic accuracy of cardiac positron emission tomography versus single photon emission computed tomography for coronary artery disease: a bivariate meta-analysis," *Circ Cardiovasc Imaging,* vol. 5, no. 6, pp. 700-7, Nov 2012, doi: 10.1161/CIRCIMAGING.112.978270.

[73] M. Horger and R. Bares, "The role of single-photon emission computed tomography/computed tomography in benign and malignant bone disease," (in eng), *Seminars in nuclear medicine,* vol. 36, no. 4, pp. 286-94, Oct 2006, doi: 10.1053/j.semnuclmed.2006.05.001.

[74] S. Kosuda *et al.*, "Does bone SPECT actually have lower sensitivity for detecting vertebral metastasis than MRI?," *Journal of nuclear medicine : official publication, Society of Nuclear Medicine,* vol. 37, no. 6, pp. 975-8, Jun 1996. [Online]. Available: https://www.ncbi.nlm.nih.gov/pubmed/8683325.

[75] T. Van den Wyngaert *et al.*, "The EANM practice guidelines for bone scintigraphy," *European journal of nuclear medicine and molecular imaging,* vol. 43, no. 9, pp. 1723-38, Aug 2016, doi: 10.1007/s00259-016-3415-4.

[76] T. B. Bartel *et al.*, "SNMMI Procedure Standard for Bone Scintigraphy 4.0," *J Nucl Med Technol,* vol. 46, no. 4, pp. 398-404, Dec 2018. [Online]. Available: https://www.ncbi.nlm.nih.gov/pubmed/30518604.

[77] A. I. Brenner, J. Koshy, J. Morey, C. Lin, and J. DiPoce, "The bone scan," *Seminars in nuclear medicine,* vol. 42, no. 1, pp. 11-26, Jan 2012, doi: 10.1053/j.semnuclmed.2011.07.005.

[78] K. K. Wong and M. Piert, "Dynamic bone imaging with 99mTc-labeled diphosphonates and 18F-NaF: mechanisms and applications," *Journal of nuclear medicine : official publication, Society of Nuclear Medicine,* vol. 54, no. 4, pp. 590-9, Apr 2013, doi: 10.2967/jnumed.112.114298.

[79] S. Usmani *et al.*, "Prospective study of Na[(18)F]F PET/CT for cancer staging in morbidly obese patients compared with [(99m)Tc]Tc-MDP whole-body planar, SPECT and SPECT/CT," *Acta Oncol,* pp. 1-10, Jul 21 2022, doi: 10.1080/0284186X.2022.2101899.

[80] E. Palma, J. D. Correia, B. L. Oliveira, L. Gano, I. C. Santos, and I. Santos, "99mTc(CO)3-labeled pamidronate and alendronate for bone imaging," *Dalton Trans,* vol. 40, no. 12, pp. 2787-96, Mar 28 2011, doi: 10.1039/c0dt01396j.

[81] L. Qiu, W. Cheng, J. Lin, S. Luo, L. Xue, and J. Pan, "Synthesis and biological evaluation of novel (99m)Tc-labelled bisphosphonates as superior bone imaging agents," *Molecules,* vol. 16, no. 8, pp. 6165-78, Jul 25 2011, doi: 10.3390/molecules16086165.

[82] P. M. Seferovic *et al.*, "Clinical practice update on heart failure 2019: pharmacotherapy, procedures, devices and patient management. An expert consensus meeting report of the Heart Failure Association of the European Society of Cardiology," *Eur J Heart Fail,* vol. 21, no. 10, pp. 1169-1186, Oct 2019, doi: 10.1002/ejhf.1531.

[83] H. O. Anger, "Scintillation Camera," *Review of Scientific Instruments,* vol. 29, no. 1, pp. 27-33, 1958, doi: 10.1063/1.1715998.

[84] D. E. Kuhl and R. Q. Edwards, "Image Separation Radioisotope Scanning," *Radiology,* vol. 80, no. 4, pp. 653-662, 1963, doi: 10.1148/80.4.653.

[85] B. H. Hasegawa, E. L. Gingold, S. M. Reilly, S.-C. Liew, and C. E. Cann, "Description of a simultaneous emission-transmission CT system," in *Medical Imaging IV: Image Formation*, R. H. Schneider, Ed., July 01, 1990 1990, vol. 1231, pp. 50-60, doi: 10.1117/12.18783. [Online]. Available: https://ui.adsabs.harvard.edu/abs/1990SPIE.1231...50H

[86] M. Bocher *et al.*, "Gamma camera-mounted anatomical X-ray tomography: technology, system characteristics and first images," (in eng), *Eur J Nucl Med,* vol. 27, no. 6, pp. 619-27, Jun 2000, doi: 10.1007/s002590050555.

[87] J. A. Patton, D. Delbeke, and M. P. Sandler, "Image fusion using an integrated, dual-head coincidence camera with X-ray tube-based attenuation maps," (in eng), *Journal of nuclear medicine : official publication, Society of Nuclear Medicine,* vol. 41, no. 8, pp. 1364-8, Aug 2000.

[88] G. Mariani and H. W. Strauss, "Positron emission and single-photon emission imaging: synergy rather than competition," *European journal of nuclear medicine and molecular imaging,* vol. 38, no. 7, pp. 1189-1190, 2011/07/01 2011, doi: 10.1007/s00259-011-1767-3.

[89] Y. Chen, M. C. Goorden, B. Vastenhouw, and F. J. Beekman, "Optimized sampling for high resolution multi-pinhole brain SPECT with stationary detectors," (in eng), *Phys Med Biol,* vol. 65, no. 1, p. 015002, Jan 10 2020, doi: 10.1088/1361-6560/ab5bc6.

[90] M. D. Walker *et al.*, "Performance assessment of a preclinical PET scanner with pinhole collimation by comparison to a coincidence-based small-animal PET scanner," *Journal of nuclear medicine : official publication, Society of Nuclear Medicine,* vol. 55, no. 8, pp. 1368-74, Aug 2014, doi: 10.2967/jnumed.113.136663.

[91] M. P. Nguyen, M. C. Goorden, C. Kamphuis, and F. J. Beekman, "Evaluation of pinhole collimator materials for micron-resolution ex vivo SPECT," *Phys Med Biol,* vol. 64, no. 10, p. 105017, May 16 2019, doi: 10.1088/1361-6560/ab1618.

[92] M. C. Goorden and F. J. Beekman, "High-resolution tomography of positron emitters with clustered pinhole SPECT," *Phys Med Biol,* vol. 55, no. 5, pp. 1265-77, Mar 7 2010, doi: 10.1088/0031-9155/55/5/001.

[93] K. Van Audenhaege, R. Van Holen, S. Vandenberghe, C. Vanhove, S. D. Metzler, and S. C. Moore, "Review of SPECT collimator selection, optimization, and fabrication for clinical and preclinical imaging," (in eng), *Medical physics,* vol. 42, no. 8, pp. 4796-813, Aug 2015, doi: 10.1118/1.4927061.

[94] J. G. Park, S. H. Jung, J. B. Kim, J. Moon, Y. S. Yeom, and C. H. Kim, "Performance evaluation of advanced industrial SPECT system with diverging collimator," *Appl Radiat Isot,* vol. 94, pp. 125-130, Dec 2014, doi: 10.1016/j.apradiso.2014.07.020.

[95] M. A. Park, S. C. Moore, and M. F. Kijewski, "Brain SPECT with short focal-length cone-beam collimation," *Medical physics,* vol. 32, no. 7Part1, pp. 2236-2244, Jul 2005, doi: 10.1118/1.1929208.

[96] R. Ter-Antonyan, R. J. Jaszczak, K. L. Greer, J. E. Bowsher, S. D. Metzler, and R. E. Coleman, "Combination of converging collimators for high-sensitivity brain SPECT," *Journal of nuclear medicine : official publication, Society of Nuclear Medicine,* vol. 50, no. 9, pp. 1548-56, Sep 2009, doi: 10.2967/jnumed.109.062653.

[97] H. R. Baghani, "Image quality parameters in brain imaging with fan-beam collimator: a Monte Carlo study on radiation scattering effects," *Radiol Phys Technol,* vol. 12, no. 2, pp. 194-200, Jun 2019, doi: 10.1007/s12194-019-00514-w.

[98] R. A. Vogel, D. Kirch, M. LeFree, and P. Steele, "A new method of multiplanar emission tomography using a seven pinhole collimator and an Anger scintillation camera," *Journal of nuclear medicine : official publication, Society of Nuclear Medicine,* vol. 19, no. 6, pp. 648-54, Jun 1978. [Online]. Available: https://www.ncbi.nlm.nih.gov/pubmed/660277.

[99] K. Vunckx, D. Beque, M. Defrise, and J. Nuyts, "Single and multipinhole collimator design evaluation method for small animal SPECT," *IEEE Trans Med Imaging,* vol. 27, no. 1, pp. 36-46, Jan 2008, doi: 10.1109/TMI.2007.902802.

[100] K. Vunckx, P. Suetens, and J. Nuyts, "Effect of overlapping projections on reconstruction image quality in multipinhole SPECT," *IEEE Trans Med Imaging,* vol. 27, no. 7, pp. 972-83, 2008, doi: 10.1109/TMI.2008.922700.

[101] K. Van Audenhaege, C. Vanhove, S. Vandenberghe, and R. Van Holen, "The evaluation of data completeness and image quality in multiplexing multi-pinhole SPECT," (in eng), *IEEE Trans Med Imaging,* vol. 34, no. 2, pp. 474-86, Feb 2015, doi: 10.1109/tmi.2014.2361051.

[102] G. S. Mok, B. M. Tsui, and F. J. Beekman, "The effects of object activity distribution on multiplexing multi-pinhole SPECT," (in eng), *Phys Med Biol,* vol. 56, no. 8, pp. 2635-50, Apr 21 2011, doi: 10.1088/0031-9155/56/8/019.

[103] J. P. Islamian, A. Azazrm, B. Mahmoudian, and E. Gharapapagh, "Advances in pinhole and multi-pinhole collimators for single photon emission computed tomography imaging," *World J Nucl Med,* vol. 14, no. 1, pp. 3-9, Jan-Apr 2015, doi: 10.4103/1450-1147.150505.

[104] M. C. Goorden, M. C. Rentmeester, and F. J. Beekman, "Theoretical analysis of full-ring multi-pinhole brain SPECT," (in eng), *Phys Med Biol,* vol. 54, no. 21, pp. 6593-610, Nov 7 2009, doi: 10.1088/0031-9155/54/21/010.

[105] K. Van Audenhaege, S. Vandenberghe, K. Deprez, B. Vandeghinste, and R. Van Holen, "Design and simulation of a full-ring multi-lofthole collimator for brain SPECT," (in eng), *Phys Med Biol,* vol. 58, no. 18, pp. 6317-36, Sep 21 2013, doi: 10.1088/0031-9155/58/18/6317.

[106] W. W. Moses, "Fundamental Limits of Spatial Resolution in PET," (in eng), *Nucl Instrum Methods Phys Res A,* vol. 648 Supplement 1, pp. S236-s240, Aug 21 2011, doi: 10.1016/j.nima.2010.11.092.

[107] M. Lukas, A. Kluge, N. Beindorff, and W. Brenner, "Multi-Isotope Capabilities of a Small-Animal Multi-Pinhole SPECT System," *Journal of nuclear medicine : official publication, Society of Nuclear Medicine,* vol. 61, no. 1, pp. 152-161, Jan 2020, doi: 10.2967/jnumed.119.226027.

[108] R. Hofstadter, "Crystal counters," *Nucleonics,* vol. 4, no. 5, p. 29; passim, May 1949. [Online]. Available: https://www.ncbi.nlm.nih.gov/pubmed/18119923.

[109] G. J. Gruber, W. W. Moses, S. E. Derenzo, N. W. Wang, E. Beuville, and H. Ho, "A discrete scintillation camera module using silicon photodiode readout of CsI(TI) crystals for breast cancer imaging," *IEEE Transactions on Nuclear Science,* vol. 45, no. 3, pp. 1063-1068, 1998, doi: 10.1109/23.681979.

[110] A. D. Guerra *et al.*, "Performance evaluation of the fully engineered YAP-(S)PET scanner for small animal imaging," *IEEE Transactions on Nuclear Science,* vol. 53, no. 3, pp. 1078-1083, 2006, doi: 10.1109/TNS.2006.871900.

[111] E. G. DePuey, "Advances in SPECT camera software and hardware: currently available and new on the horizon," (in eng), *Journal of nuclear cardiology : official publication of the American Society of Nuclear Cardiology,* vol. 19, no. 3, pp. 551-81; quiz 585, Jun 2012, doi: 10.1007/s12350-012-9544-7.

[112] H. Shiraki, M. Funaki, Y. Ando, A. Tachibana, S. Kominami, and R. Ohno, "THM Growth and Characterization of 100 mm Diameter CdTe Single Crystals," *IEEE Transactions on Nuclear Science,* vol. 56, no. 4, pp. 1717-1723, 2009, doi: 10.1109/TNS.2009.2016843.

[113] P. J. Slomka, R. J. H. Miller, L. H. Hu, G. Germano, and D. S. Berman, "Solid-State Detector SPECT Myocardial Perfusion Imaging," *Journal of nuclear medicine : official publication, Society of Nuclear Medicine,* vol. 60, no. 9, pp. 1194-1204, Sep 2019, doi: 10.2967/jnumed.118.220657.

[114] S. Dorbala *et al.*, "Single Photon Emission Computed Tomography (SPECT) Myocardial Perfusion Imaging Guidelines: Instrumentation, Acquisition, Processing, and Interpretation," *Journal of nuclear cardiology : official publication of the American Society of Nuclear Cardiology,* vol. 25, no. 5, pp. 1784-1846, Oct 2018, doi: 10.1007/s12350-018-1283-y.

[115] P. J. Slomka, D. S. Berman, and G. Germano, "New cardiac cameras: single-photon emission CT and PET," *Seminars in nuclear medicine,* vol. 44, no. 4, pp. 232-51, Jul 2014, doi: 10.1053/j.semnuclmed.2014.04.003.

[116] J. S. Lee, G. Kovalski, T. Sharir, and D. S. Lee, "Advances in imaging instrumentation for nuclear cardiology," *Journal of nuclear cardiology : official publication of the American Society of Nuclear Cardiology,* vol. 26, no. 2, pp. 543-556, Apr 2019, doi: 10.1007/s12350-017-0979-8.

[117] J. A. Kennedy, I. Reizberg, R. Lugassi, S. Himmelman, and Z. Keidar, "Absolute radiotracer concentration measurement using whole-body solid-state SPECT/CT technology: in vivo/in vitro validation," *Med Biol Eng Comput,* vol. 57, no. 7, pp. 1581-1590, Jul 2019, doi: 10.1007/s11517-019-01979-y.

[118] P. P. Bruyant, "Analytic and iterative reconstruction algorithms in SPECT," *Journal of nuclear medicine : official publication, Society of Nuclear Medicine,* vol. 43, no. 10, pp. 1343-58, Oct 2002. [Online]. Available: https://www.ncbi.nlm.nih.gov/pubmed/12368373.

[119] D. B. Kay, J. W. Keyes, Jr., and W. Simon, "Radionuclide tomographic image reconstruction using Fourier transform techniques," *Journal of nuclear medicine : official publication, Society of Nuclear Medicine,* vol. 15, no. 11, pp. 981-6, Nov 1974. [Online]. Available: https://www.ncbi.nlm.nih.gov/pubmed/4422987.

[120] L. A. Shepp and Y. Vardi, "Maximum likelihood reconstruction for emission tomography," *IEEE Trans Med Imaging,* vol. 1, no. 2, pp. 113-22, 1982, doi: 10.1109/TMI.1982.4307558.

[121] K. Lange and R. Carson, "EM reconstruction algorithms for emission and transmission tomography," (in eng), *J Comput Assist Tomogr,* vol. 8, no. 2, pp. 306-16, Apr 1984.

[122] H. M. Hudson and R. S. Larkin, "Accelerated image reconstruction using ordered subsets of projection data," *IEEE Trans Med Imaging,* vol. 13, no. 4, pp. 601-9, 1994, doi: 10.1109/42.363108.

[123] B. F. Hutton, "Recent advances in iterative reconstruction for clinical SPECT/PET and CT," *Acta Oncologica,* vol. 50, no. 6, pp. 851-858, 2011/08/01 2011, doi: 10.3109/0284186X.2011.580001.

[124] W. Branderhorst, B. Vastenhouw, and F. J. Beekman, "Pixel-based subsets for rapid multi-pinhole SPECT reconstruction," *Phys Med Biol,* vol. 55, no. 7, pp. 2023-34, Apr 7 2010, doi: 10.1088/0031-9155/55/7/015.

[125] P. E. Vaissier, M. C. Goorden, A. B. Taylor, and F. J. Beekman, "Fast Count-Regulated OSEM Reconstruction With Adaptive Resolution Recovery," *IEEE Trans Med Imaging,* vol. 32, no. 12, pp. 2250-61, Dec 2013, doi: 10.1109/TMI.2013.2279851.

[126] *National Electrical Manufacturers Association in NEMA Standards Publication NU 4-2008: Performance Measurements of Small Animal Positron Emission Tomographs*. Rosslyn (VA), 2008.

[127] D. R. Osborne, C. Kuntner, S. Berr, and D. Stout, "Guidance for Efficient Small Animal Imaging Quality Control," (in eng), *Molecular imaging and biology : MIB : the official publication of the Academy of Molecular Imaging,* vol. 19, no. 4, pp. 485-498, 2017, doi: 10.1007/s11307-016-1012-3.

[128] J. G. Mannheim *et al.*, "Standardization of Small Animal Imaging—Current Status and Future Prospects," *Molecular Imaging and Biology,* journal article vol. 20, no. 5, pp. 716-731, October 01 2018, doi: 10.1007/s11307-017-1126-2.

[129] L. S. Chow and R. Paramesran, "Review of medical image quality assessment," *Biomedical Signal Processing and Control,* vol. 27, pp. 145-154, 2016/05/01/ 2016, doi: https://doi.org/10.1016/j.bspc.2016.02.006.

[130] P. Mohammadi, A. Ebrahimi-Moghadam, and S. Shirani, "Subjective and objective quality assessment of image: A survey," *arXiv preprint arXiv:1406.7799,* 2014.

[131] Z. Wang, "Applications of Objective Image Quality Assessment Methods [Applications Corner]," *IEEE Signal Processing Magazine,* vol. 28, no. 6, pp. 137-142, 2011, doi: 10.1109/MSP.2011.942295.

[132] F. J. Beekman *et al.*, "U-SPECT-I: a novel system for submillimeter-resolution tomography with radiolabeled molecules in mice," *Journal of nuclear medicine : official publication, Society of Nuclear Medicine,* vol. 46, no. 7, pp. 1194-200, Jul 2005. [Online]. Available: https://www.ncbi.nlm.nih.gov/pubmed/16000289.

[133] MILabs B.V., *User Manual: U-SPECT$^5$ U-SPECT5CT U-PET5 U-PET5CT U-CT VECTor5 VECTor5CT*, Utrecht, The Netherlands: MILabs B.V., 2018.

[134] P. E. Vaissier, M. C. Goorden, B. Vastenhouw, F. van der Have, R. M. Ramakers, and F. J. Beekman, "Fast spiral SPECT with stationary gamma-cameras and focusing pinholes," *Journal of nuclear medicine : official publication, Society of Nuclear Medicine,* vol. 53, no. 8, pp. 1292-9, Aug 2012, doi: 10.2967/jnumed.111.101899.

[135] K. Ogawa, Y. Harata, T. Ichihara, A. Kubo, and S. Hashimoto, "A practical method for position-dependent Compton-scatter correction in single photon emission CT," *IEEE Trans Med Imaging,* vol. 10, no. 3, pp. 408-12, 1991, doi: 10.1109/42.97591.

[136] A. M. Loening and S. S. Gambhir, "AMIDE: a free software tool for multimodality medical image analysis," *Mol Imaging,* vol. 2, no. 3, pp. 131-7, Jul 2003, doi: 10.1162/153535003322556877.

[137] *Technetium-99m Radiopharmaceuticals: Manufacture of Kits*. Vienna: International Atomic Energy Agency, 2008.

[138] C. National Research Council Committee for the Update of the Guide for the and A. Use of Laboratory, "The National Academies Collection: Reports funded by National Institutes of Health," in *Guide for the Care and Use of Laboratory Animals*. Washington (DC): National Academies Press (US)
Copyright © 2011, National Academy of Sciences., 2011.

[139] G. Arsos *et al.*, "(99m)Tc-sestamibi uptake in rat skeletal muscle and heart: physiological determinants and correlations," *Physiol Res,* vol. 58, no. 1, pp. 21-28, 2009, doi: 10.33549/physiolres.931327.

[140] G. C. Urbaniak and S. Plous. "Research Randomizer (Version 4.0)." http://www.randomizer.org/ (accessed 16.05.2020, 2020).

[141] E. Prieto *et al.*, "Performance evaluation of a preclinical SPECT/CT system for multi-animal and multi-isotope quantitative experiments," *Scientific Reports,* vol. 12, no. 1, p. 18161, 2022/10/28 2022, doi: 10.1038/s41598-022-21687-2.

[142] F. Boisson *et al.*, "Imaging capabilities of the Inveon SPECT system using single- and multipinhole collimators," *Journal of nuclear medicine : official publication, Society of Nuclear Medicine,* vol. 54, no. 10, pp. 1833-40, Oct 2013, doi: 10.2967/jnumed.112.117572.

[143] N. U. Schramm, C. Lackas, B. Gershman, J. P. Norenberg, and M. deJong, "Improving resolution, sensitivity and applications for the NanoSPECT/CT: A high-performance SPECT/CT imager for small-animal research," (in English), *European journal of nuclear medicine and molecular imaging,* vol. 34, pp. S226-S227, Oct 2007. [Online]. Available: <Go to ISI>://WOS:000253283900511.

[144] M. J. Combs, B. Y. Croft, and J. Arora, "Biodistribution of TC-99m sestamibi in rats utilizing whole-body autoradiography," (in English), vol. 35, 1994-05-01 1994, doi: Journal Name: Journal of Nuclear Medicine; Journal Volume: 35; Journal Issue: Suppl.5; Conference: 41. annual meeting of the Society of Nuclear Medicine, Orlando, FL (United States), 5-8 Jun 1994; Other Information: PBD: May 1994.

[145] J. V. Hoffmann *et al.*, "Performance evaluation of fifth-generation ultra-high-resolution SPECT system with two stationary detectors and multi-pinhole imaging," *EJNMMI Physics,* vol. 7, no. 1, p. 64, 2020/11/02 2020, doi: 10.1186/s40658-020-00335-6.

[146] V. Moji *et al.*, "Performance evaluation of a newly developed high-resolution, dual-head animal SPECT system based on the NEMA NU1-2007 standard," (in eng), *Journal of applied clinical medical physics,* vol. 15, no. 6, p. 4936, Nov 2014, doi: 10.1120/jacmp.v15i6.4936.

[147] Y. Matsusaka *et al.*, "Performance Evaluation of a Preclinical SPECT Scanner with a Collimator Designed for Medium-Sized Animals," *Molecular Imaging,* vol. 2022, p. 9810097, 2022/07/16 2022, doi: 10.1155/2022/9810097.

[148] A. L. Goertzen *et al.*, "NEMA NU 4-2008 comparison of preclinical PET imaging systems," (in eng), *Journal of nuclear medicine : official publication, Society of Nuclear Medicine,* vol. 53, no. 8, pp. 1300-9, Aug 2012, doi: 10.2967/jnumed.111.099382.

[149] E. J. Meester *et al.*, "Perspectives on Small Animal Radionuclide Imaging; Considerations and Advances in Atherosclerosis," (in eng), *Front Med (Lausanne),* vol. 6, p. 39, 2019, doi: 10.3389/fmed.2019.00039.

[150] M. C. Goorden, C. Kamphuis, R. M. Ramakers, and F. J. Beekman, "Accelerated image reconstruction by a combined dual-matrix dual-voxel approach," (in eng), *Phys Med Biol,* vol. 65, no. 10, p. 105014, Jun 9 2020, doi: 10.1088/1361-6560/ab82e9.

# Appendix

# I List of Abbreviations

$^{18}$F-FDG ..... *fluorine-18 fluorodeoxyglucose*
$^{18}$F-NaF ..... *fluorine-18 sodium fluoride*
2D ..... *two-dimensional*
3D ..... *three-dimensional*
$^{99m}$Tc-HMDP ..... *technetium-99m hydroxymethylene diphosphonate*
$^{99m}$Tc-MDP ..... *technetium-99m methyl diphosphonate*
$^{99m}$Tc-MIBI ..... *technetium-99m sesta-methoxyisobutylisonitrile*
BP ..... *bed position*
CAD-RADS ..... *coronary artery disease reporting and data system*
CFOV ..... *central field of view*
CR-OSEM ..... *count-regulated ordered subsets expectation maximization*
CsI(Tl) ..... *thallium-doped cesium iodide*
CT ..... *computed tomography*
CZT ..... *cadmium-zinc telluride*
ESC ..... *european society of cardiology*
FBP ..... *filtered back projection*
FOV ..... *field of view*
FWHM ..... *full width at half maximum*
HLA ..... *horizontal long axis*
IAEA ..... *International Atomic Energy Association*
IQ score ..... *image quality score*
IQR ..... *interquartile range*
MIP ..... *maximum intensity projection*
MLEM ..... *maximum likelihood expectation maximization*
MRI ..... *magnetic resonance imaging*
NaI(Tl) ..... *thallium-doped sodium iodide*
NEMA ..... *National Electrical Manufacturers Association*
NIfTI ..... *Neuroimaging Informatics Technology Initiative*
OSEM ..... *ordered-subsets expectation maximization*
PET ..... *positron emission tomography*
PMT ..... *photo multiplier tube*
ROI ..... *region of interest*
SA ..... *short axis*
SPECT ..... *single-photon emission computed tomography*
SROSEM ..... *similarity-regulated ordered-subsets expectation maximization*
TPB ..... *time per bed position*
TT ..... *translation time*
UHR-RM ..... *ultra-high resolution rat/mouse collimator*
VLA ..... *vertical long axis*

# II List of Figures

# III List of Tables

# IV Acknowledgment

First and foremost, I would like to thank Prof. Dr. Andreas Buck, Head of the Department of Nuclear Medicine, and his entire team, because it was only because of you that I was able to complete my doctoral thesis in the field of nuclear medicine. Furthermore, I would like to thank the Graduate School of Life Sciences for the generous support and close supervision in their Medical Doctoral Researchers Program.

Prof. Dr. Takahiro Higuchi, from the Department of Molecular Imaging of the Comprehensive Heart Failure Center in Würzburg, introduced me to the broad field of molecular imaging. He always supported me with advice and total commitment and took the time to discuss any questions. I am delighted to have found such a good and competent supervisor, and I thank him wholeheartedly.

I would also like to thank Prof. Dr. Herbert Köstler and Dr. Jan-Peter Grunz, from the Department of Radiology at the University Hospital of Würzburg. They have enriched the project with their expertise and an interdisciplinary perspective.

My special thanks go to Jan Vincent Hoffmann, with whom I carried out all projects and scientific experiments. He was a constant companion; we worked together on the research questions, experimental design, and implementation. Without him, the publications underlying this work would not have been possible in the present form.
Takayuki Kanno worked with us as a Japanese exchange scientist and contributed many helpful ideas to the project. As laboratory administrator, Lars Mayer helped us to find our way around, especially in the beginning, and enabled us to get started with the scientific work in the laboratory. In addition to those mentioned, I would also like to thank the other working group members. Of course, you all contributed to an incredibly great time.

At this point, I would also like to mention the exchange program with Kanazawa University in Japan and thank the Department of Nuclear Medicine of the University Hospital Würzburg for funding my research stay. The supervision in Japan by Prof. Dr. Seigo Kinuya and his staff in the Department of Nuclear Medicine at Kanazawa University Hospital was excellent. I will never forget the Japanese hospitality. This is where I would like to mention Dr. Saito, Dr. Wakabayashi, and Dr. Kayano from the Department of Nuclear Medicine, who made the time an unforgettable experience. My

special thanks also go to the head of the laboratory, Prof. Onoguchi, and his colleague Dr. Shibutani.

Finally, I would like to thank my parents, friends, and my entire social environment, who have always supported me during medical school and the completion of my doctoral thesis. Thank you all very much.

# Danksagung

In erster Linie möchte ich mich bei Herrn Prof. Dr. Andreas Buck, Leiter der Klinik und Poliklinik für Nuklearmedizin und seinem gesamten Team bedanken, denn nur durch Sie war es mir möglich, meine Doktorarbeit auf dem Gebiet der Nuklearmedizin abzuschließen. Weiterhin möchte ich mich bei der Graduate School of Life Sciences für die großzügige Unterstützung und enge Betreuung in ihrem Medical Doctoral Researchers Program bedanken.

Prof. Dr. Takahiro Higuchi von der Abteilung für Molekulare Bildgebung des Deutschen Zentrums für Herzinsuffizienz in Würzburg hat mich in das weite Feld der molekularen Bildgebung eingeführt. Er stand mir stets mit Rat und vollem Engagement zur Seite und nahm sich die Zeit, alle aufkommenden Fragen zu besprechen. Ich bin sehr froh, einen so guten und kompetenten Betreuer gefunden zu haben und danke ihm von ganzem Herzen.

Außerdem möchte ich mich bei Prof. Dr. Köstler und Dr. J.-P. Grunz von der Radiologischen Klinik des Universitätsklinikums Würzburg, die das Projekt mit ihrer Expertise und einem anderen Blickwinkel bereichert haben.

Mein besonderer Dank gilt Jan Vincent Hoffmann, mit dem ich alle Projekte und wissenschaftlichen Experimente gemeinsam durchgeführt habe. Er war ein ständiger Begleiter und wir haben gemeinsam an den Forschungsfragen, der Versuchsplanung und der Durchführung gearbeitet. Ohne ihn wären die Publikationen, auf denen diese Dissertationsschrift basiert, in der vorliegenden Form nicht möglich gewesen.

Takayuki Kanno hat als japanischer Austauschwissenschaftler mit uns gearbeitet und viele hilfreiche Ideen in das Projekt eingebracht. Lars Mayer als Laboradministrator hat uns vor allem am Anfang geholfen, uns zurechtzufinden, und hat uns ermöglicht, schnell mit der wissenschaftlichen Arbeit im Labor zu beginnen. Neben den Genannten möchte ich mich auch bei den anderen Mitgliedern der Arbeitsgruppe bedanken. Sie alle haben zu einer unglaublich großartigen Zeit beigetragen.

An dieser Stelle möchte ich auch das Austauschprogramm mit der Kanazawa Universität in Japan erwähnen und mich bei der Klinik für Nuklearmedizin des Universitätsklinikums

Würzburg für die Finanzierung meines Aufenthaltes bedanken. Die Betreuung in Japan durch Prof. Dr. Seigo Kinuya und seine Mitarbeiter in der Abteilung für Nuklearmedizin am Universitätsklinikum Kanazawa war hervorragend, und die japanische Gastfreundschaft wird mir immer in Erinnerung bleiben. An dieser Stelle möchte ich Dr. Saito, Dr. Wakabayashi und Dr. Kayano von der Abteilung für Nuklearmedizin erwähnen, die die Zeit zu einem unvergesslichen Erlebnis machten. Mein besonderer Dank gilt auch dem Leiter des Labors Prof. Onoguchi und seinem Kollegen Dr. Shibutani.

Schließlich möchte ich mich bei meinen Eltern und Freunden sowie meinem gesamten sozialen Umfeld bedanken, die mich während meiner Zeit als Medizinstudent und bei der Erstellung meiner Doktorarbeit immer unterstützt haben. Herzlichen Dank!

# V Publications and Congress Attendances

**Publications:**

1. Janssen JP, Hoffmann JV, Kanno T, et al. Capabilities of multi-pinhole SPECT with two stationary detectors for in vivo rat imaging. Sci Rep. 2020;10(1):18616.

2. Hoffmann JV, Janssen JP, Kanno T, et al. Performance evaluation of fifth-generation ultra-high-resolution SPECT system with two stationary detectors and multi-pinhole imaging. EJNMMI Physics. 2020;7(1):64.

**Congress Attendances:**

1. Janssen JP, Hoffmann JV, Kanno T, Higuchi T. Capabilities of multi-pinhole SPECT as a tool for preclinical in-vivo rat imaging. Poster presented at European Molecular Imaging Meeting - EMIM 2020; 26$^{th}$ August 2020; Virtual Edition.

2. Janssen JP, Hoffmann JV, Kanno T, Higuchi T. Multi-pinhole SPECT Imaging of Rat Hearts and Bones: Image Quality under In Vivo Conditions. Oral Presentation presented at 33rd Annual Congress of the European Association of Nuclear Medicine - EANM'20; 30$^{th}$ October 2020; Virtual Edition.

# VI Affidavit

I hereby confirm that my thesis *"Capabilities of a multi-pinhole SPECT system with two stationary detectors for in vivo imaging in rodents"* is the result of my own work. I did not receive any help or support from commercial consultants. All sources and / or materials applied are listed and specified in the thesis.

Furthermore, I confirm that this thesis has not yet been submitted as part of another examination process neither in identical nor in similar form.

Place, Date Signature

# Eidesstattliche Erklärung

Hiermit erkläre ich an Eides statt, die Dissertation *„Leistungsfähigkeit eines Multi-Pinhole SPECT-Systems mit zwei stationären Detektoren zur In-vivo-Bildgebung in Nagetiermodellen"* eigenständig, d.h. insbesondere selbständig und ohne Hilfe eines kommerziellen Promotionsberaters, angefertigt und keine anderen als die von mir angegebenen Quellen und Hilfsmittel verwendet zu haben.

Ich erkläre außerdem, dass die Dissertation weder in gleicher noch in ähnlicher Form bereits in einem anderen Prüfungsverfahren vorgelegen hat.

Ort, Datum Unterschrift

# VII Curriculum Vitae